


FULL PAPER

Open Access



Electrical conductivity of old oceanic mantle in the northwestern Pacific I: 1-D profiles suggesting differences in thermal structure not predictable from a plate cooling model

Kiyoshi Baba^{1*} , Noriko Tada^{1,2}, Tetsuo Matsuno^{1,3}, Pengfei Liang¹, Ruibai Li¹, Luolei Zhang⁴, Hisayoshi Shimizu¹, Natsue Abe⁵, Naoto Hirano⁶, Masahiro Ichiki⁷ and Hisashi Utada¹

Abstract

Seafloor magnetotelluric (MT) experiments were recently conducted in two areas of the northwestern Pacific to investigate the nature of the old oceanic upper mantle. The areas are far from any tectonic activity, and “normal” mantle structure is therefore expected. The data were carefully analyzed to reduce the effects of coastlines and seafloor topographic changes, which are significant boundaries in electrical conductivity and thus distort seafloor MT data. An isotropic, one-dimensional electrical conductivity profile was estimated for each area. The profiles were compared with those obtained from two previous study areas in the northwestern Pacific. Between the four profiles, significant differences were observed in the thickness of the resistive layer beyond expectations based on cooling of homogeneous oceanic lithosphere over time. This surprising feature is now further clarified from what was suggested in a previous study. To explain the observed spatial variation, dynamic processes must be introduced, such as influence of the plume associated with the formation of the Shatsky Rise, or spatially non-uniform, small-scale convection in the asthenosphere. There is significant room of further investigation to determine a reasonable and comprehensive interpretation of the lithosphere–asthenosphere system beneath the northwestern Pacific. The present results demonstrate that electrical conductivity provides key information for such investigation.

Keywords: Geomagnetic induction, Marine magnetotellurics, Electrical conductivity, Oceanic lithosphere and asthenosphere, Northwestern Pacific

Background

The northwestern part of the Pacific Plate is composed of some of the oldest oceanic lithosphere on the planet. The history of its growth has been studied based on geomagnetic anomalies, which have indicated that the Pacific Plate began in a small triangular region at about 190 Ma; this oldest part of the plate is now located in the East Mariana Basin (Nakanishi et al. 1992). The seafloor off the Japanese islands formed 120–160 Ma through the spreading of the Pacific-Izanagi Ridge system, which

has already been subducted into the mantle via the Kuril-Japan-Izu-Bonin Trenches. A large bathymetric high called the Shatsky Rise is thought to have formed through upwelling from deep in the mantle or decompression melting of chemically heterogeneous asthenosphere near the Pacific-Izanagi-Farallon triple junction between 149 and 124 Ma (e.g., Sager 2005). The seafloor surrounding the Shatsky Rise is relatively flat and is more than 5600 m deep, which is deeper than predicted by the model of Stein and Stein (1992) based on the cooling rate of a thermally conductive plate of finite thickness (Korenaga and Korenaga 2008).

The structure of the mantle beneath such an old ocean basin can be investigated using geophysical approaches.

*Correspondence: kbaba@eri.u-tokyo.ac.jp

¹ Earthquake Research Institute, The University of Tokyo, 1-1-1, Yayoi, Bunkyo-ku, Tokyo 113-0032, Japan

Full list of author information is available at the end of the article

Old oceanic lithosphere is generally believed to be thicker than younger oceanic lithosphere because of cooling over time. Many global surface wave tomography studies have demonstrated clear age-dependence of shear-wave velocity structure (e.g., Maggi et al. 2006; Nettles and Dziewonski 2008; Burgos et al. 2014), and the high-velocity lid, which is interpreted as cool lithosphere, is imaged to be as thick as 100–150 km in the northwestern Pacific, although the structure beneath the specific area of interest for this study has not been resolved in detail through such global studies. A local study using seismic receiver functions detected with a borehole seismometer in the northwestern Pacific revealed a sharp change (decreasing with depth) in seismic P- and S-wave velocities at ~82 km depth, which is thought to represent the lithosphere–asthenosphere boundary (LAB) (Kawakatsu et al. 2009). Note that LAB depth estimates are not consistent among different seismic proxies, such as changes in velocity based on tomography or receiver function, or changes in radial or azimuthal anisotropy (e.g., Burgos et al. 2014). The age-dependent evolution of both the lithosphere and the asthenosphere should be regarded as a part of a system (e.g., Kawakatsu and Utada 2017). From this perspective, the nature of the oceanic lithosphere–asthenosphere system (LAS), for example, the relation between the evolving thermal structure and mechanical properties, is not yet fully understood based on seismic imaging methods.

Knowledge of the oceanic LAS from electrical images has been even more limited than those from seismic studies. Recently, we carried out the normal oceanic mantle (NOMan) project (<http://www.eri.u-tokyo.ac.jp/yesman/>), which aimed to investigate the state of the old Pacific mantle via marine seismic and electromagnetic (EM) observations. Baba et al. (2013a) analyzed magnetotelluric (MT) data obtained by the pilot survey and generated a preliminary one-dimensional (1-D) electrical conductivity profile for the upper mantle, which shows that the resistive lithospheric mantle is as thick as ~80 km. One important finding was that the resistive layer in this area of the lithosphere is unexpectedly different from that detected in the area off the Bonin Trench (Baba et al. 2010), although the lithospheric ages differ little between the two areas. This finding suggests a breakdown of the simple lithospheric cooling concept.

The main phase of observation under the NOMan project began in 2011 and continued to 2015; a great deal of additional data are now available. In this paper, we present a comprehensive report on the EM part of the NOMan project. First, we introduce the datasets and 1-D conductivity profiles for the upper mantle, which are newly obtained for two areas: the northwest and the southeast of the Shatsky Rise. Compared with the dataset

used by Baba et al. (2013a), (1) the number of observation sites was increased and the area covered is wider, (2) the data were collected from an additional area to examine the generality of structural features, and (3) the period range to be analyzed was extended to include both shorter and longer periods and thus yields more constraints for shallower and deeper structures. We discuss the features of the LAS beneath the northwestern Pacific by comparing the 1-D profiles from the NOMan project with those obtained with similar methods from the other two areas in the northwestern Pacific where data were acquired in past experiments (Baba et al. 2010, 2013b).

Methods

Field experiments and data

For the NOMan project, EM and seismic observations have been conducted since 2010. Here, we summarize the EM observations and data. Two survey areas were selected for this research: northwest (Area A) and southeast (Area B) of the Shatsky Rise (Fig. 1). Both areas have relatively flat seafloor as old as 130–145 Ma. Korenaga and Korenaga (2008) defined the normal seafloor as regions uncorrelated with anomalous crust. Our study areas have mostly normal seafloor according to this definition. Therefore, the mantle underneath is expected to be “normal” in the sense that the plate has cooled over time without effects from tectonic events since its formation at the spreading ridge. We originally intended to compare the two areas to examine the generality of the “normal” mantle state. Observations were initiated at five sites (NM01–NM05) in Area A as a pilot survey (Baba et al. 2013a), after which iterative deployments and retrievals of instruments in the two areas were performed each year through the main observation phase until 2015. A total of seven cruises were carried out for this experiment using the R/V *KAIRES* of the Japan Agency for Marine Science and Technology (JAMSTEC) and the W/V *KAIYU* of Offshore Operation Co., Ltd. The arrays consisted of 17 sites (labeled NM01–NM17) in Area A and eight sites (NM18–NM25) in Area B. A total of 39 EM instruments were deployed in the two areas, and most were successfully retrieved with usable data. The available time series length is at least 275 days (~9.2 months) at some sites, and, because of the iterative observation, the maximum duration of observation was 1348 days (~3.7 years) at NM01. Table 1 lists the coordinates of the sites and the status of the associated data. High-resolution bathymetry around each seafloor site, which is used for electrical conductivity modeling, was surveyed using the shipboard multi-narrow beam echo sounding (MBES) system during the *KAIRES* cruises. We compiled all available bathymetry data published by JAMSTEC in addition to those collected through the

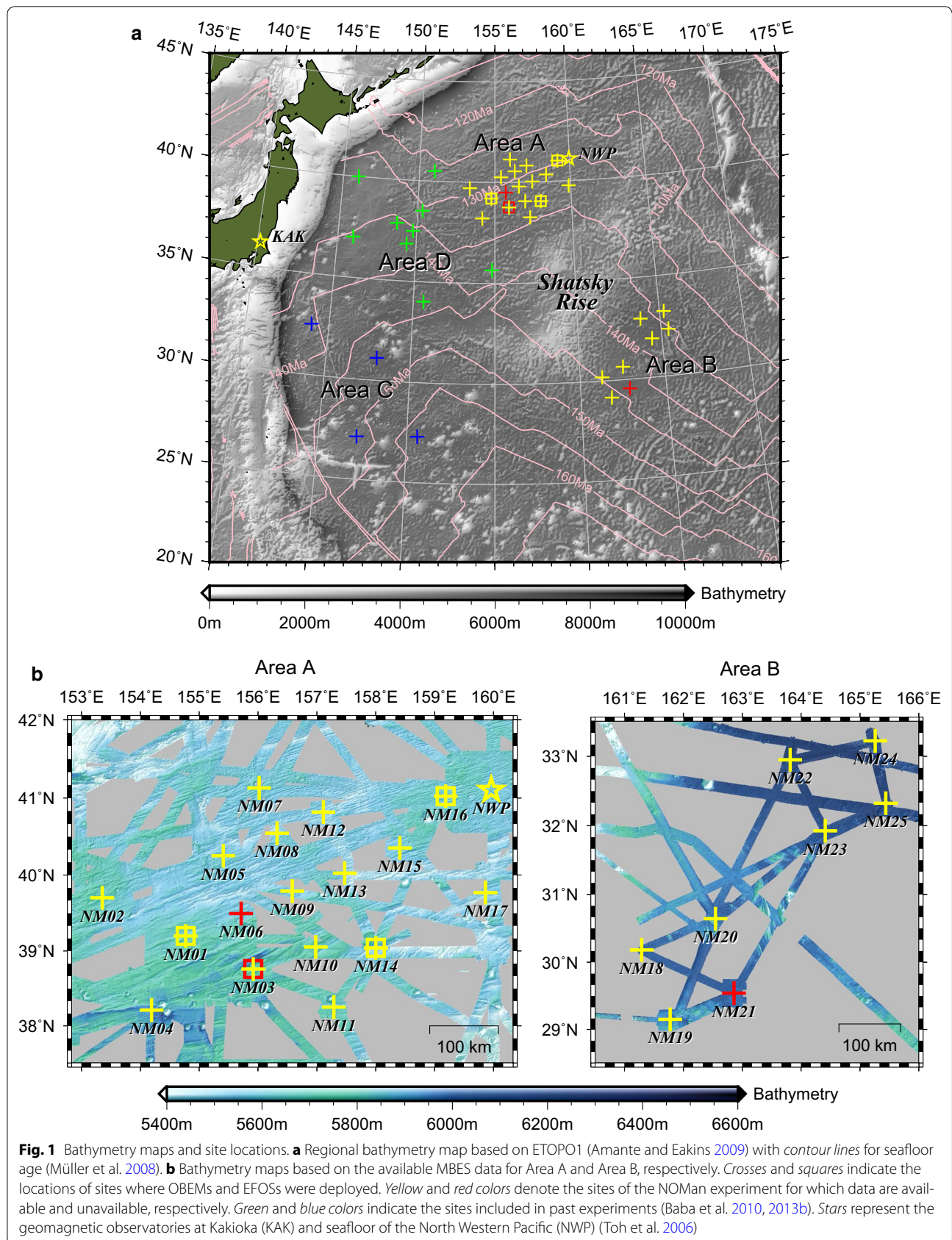


Table 1 Information on the OBEM and EFOS sites and data used in this study

Site ID	Instrument	Institute	Observation phase	Latitude	Longitude	Depth (m)	Sampling interval (s)	Available period/remarks
NM01	OBEM	ERI	Pilot	39°12.01'N	154°47.09'E	5756	60	20/06/2010–07/03/2012
		ERI	2nd	39°11.93'N	154°45.88'E	5751	60	05/09/2012–22/08/2013
		ERI	3rd	39°11.79'N	154°45.67'E	5751	10, 60 ^a	31/08/2013–06/09/2014
			<i>Average</i>	39°11.91'N	154°46.21'E	5754		
	EFOS	ERI	2nd	39°12.02'N	154°45.91'E	5748	1	10/09/2012–13/09/2014 ^b E-dipole: 1.8 km, N113°E
NM02	OBEM	ERI	Pilot	39°42.09'N	153°21.17'E	5734	60	25/06/2010–26/02/2012
		JAMSTEC	2nd	39°42.68'N	153°21.21'E	5730	60	Unavailable ^c
NM03	OBEM	ERI	Pilot	38°45.84'N	155°54.73'E	5765	60	Unavailable ^d
		ERI	2nd	38°45.03'N	155°54.06'E	5757	10, 60 ^a	Unavailable ^d
		ERI	4th	38°45.58'N	155°55.15'E	5763	10, 60 ^a	24/09/2014–13/09/2015
	EFOS	ERI	Pilot	38°45.81'N	155°54.69'E	5766	1	Unavailable ^e
			2nd	38°45.81'N	155°54.69'E	5766	1	Unavailable ^e E-dipole: 3.3 km, N111°E
NM04	OBEM	ERI	Pilot	38°12.67'N	154°11.40'E	5946	60	20/06/2010–26/11/2011
		ERI	1st	38°12.78'N	154°12.21'E	5956	10, 60 ^a	Unavailable ^d
NM05	OBEM	ERI	Pilot	40°15.00'N	155°24.40'E	5615	60	25/06/2010–26/02/2012
		ERI	2nd	40°15.22'N	155°24.78'E	5619	10, 60 ^a	21/08/2012–24/08/2013
			<i>Average</i>	40°15.11'N	155°24.59'E	5621		
NM06	OBEM	ERI	3rd	39°29.62'N	155°42.82'E	5599	10, 60 ^a	Unavailable ^d
NM07	OBEM	ERI	3rd	41°07.73'N	156°01.15'E	5632	10, 60 ^a	31/08/2013–04/06/2014
NM08	OBEM	ERI	3rd	40°32.67'N	156°19.35'E	5546	10, 60 ^a	31/08/2013–03/06/2014
NM09	OBEM	ERI	3rd	39°47.35'N	156°34.84'E	5547	10, 60 ^a	31/08/2013–02/06/2014
NM10	OBEM	ERI	3rd	39°03.19'N	156°58.83'E	5734	10, 60 ^a	31/08/2013–02/06/2014
NM11	OBEM	ERI	3rd	38°15.05'N	157°17.31'E	5704	10, 60 ^a	31/08/2013–02/06/2014
NM12	OBEM	JAMSTEC	2nd	40°49.04'N	157°06.58'E	5511	60	30/08/2012–26/08/2013
NM13	OBEM	ERI	3rd	40°01.51'N	157°28.38'E	5535	10, 60 ^a	31/08/2013–06/06/2014
NM14	OBEM	JAMSTEC	2nd	39°02.44'N	158°00.76'E	5512	10, 60 ^a	Unavailable ^e
		ERI	3rd	39°02.48'N	158°00.12'E	5510	10, 60 ^a	31/08/2013–15/09/2014
	EFOS	ERI	2nd	39°02.64'N	158°00.61'E	5509	1	06/09/2012–18/09/2014 ^b E-dipole: 2.0 km, N107°E
NM15	OBEM	JAMSTEC	2nd	40°21.17'N	158°24.51'E	5578	60	28/08/2012–27/08/2013
NM16	OBEM	ERI	2nd	41°01.33'N	159°11.19'E	5577	10, 60 ^a	27/08/2012–27/07/2014
	EFOS	ERI	2nd	41°01.27'N	159°11.20'E	5578	1	04/09/2012–17/09/2014 E-dipole: 1.9 km, N103°E
NM17	OBEM	JAMSTEC	3rd	39°46.15'N	159°51.75'E	5541	60	01/09/2013–06/06/2014
NM18	OBEM	ERI	1st	30°10.96'N	161°17.44'E	5983	60	01/12/2011–18/01/2013
NM19	OBEM	ERI	1st	29°09.09'N	161°46.51'E	5930	60	01/12/2011–02/09/2013
NM20	OBEM	JAMSTEC	1st	30°38.50'N	162°32.72'E	5970	60	01/12/2011–01/09/2013
		ERI	3rd	30°38.58'N	162°33.67'E	5968	60	Unavailable ^e
NM21	OBEM	ERI	1st	29°32.51'N	162°51.55'E	5986	60	Unavailable ^d
NM22	OBEM	JAMSTEC	1st	32°56.94'N	163°48.85'E	6188	60	01/12/2011–30/08/2013
NM23	OBEM	JAMSTEC	1st	31°55.52'N	164°24.57'E	6073	60	01/12/2011–31/08/2013
NM24	OBEM	ERI	1st	33°13.24'N	165°15.65'E	6118	60	01/12/2011–27/08/2013 ^b
		ERI	3rd	33°13.29'N	165°15.42'E	6122	10, 60 ^a	10/09/2013–17/09/2014
			<i>Average</i>	33°13.26'N	165°15.54'E	6121		

Table 1 continued

Site ID	Instrument	Institute	Observation phase	Latitude	Longitude	Depth (m)	Sampling interval (s)	Available period/remarks
NM25	OBEM	ERI	<i>1st</i>	<i>32°19.47'N</i>	<i>165°26.31'E</i>	6109	60	01/12/2011–20/03/2013

For EFOS data, the position is that of the recorder, and the dipole length and direction from the recorder are noted in remarks. The positions given in italicized characters are the representative positions for each site. Water depths at each site were retrieved from the up-to-date compilation of available MBES data, and the values for some sites are therefore slightly different from those previously reported by Baba et al. (2010, 2013a)

^a Sampling intervals were changed during observation (see text for details)

^b Includes unavailable sections

^c Failed to retrieve data

^d Failed to retrieve the instrument

^e Noisy

NOMan project cruises. The bathymetry map based on the MBES data is also shown in Fig. 1b.

Two kinds of EM instruments were utilized in this experiment: ocean bottom electromagnetometers (OBEMs) and electric field observation systems (EFOSs). OBEMs measure the time variations of three components of the magnetic field, two horizontal components of the electric field, two components of instrumental tilt, and temperature. These instruments were deployed to the seafloor via free fall from the sea surface and were retrieved when they rose to the surface due to buoyancy after releasing an anchor. Most of the OBEMs recorded data with a sampling interval of 60 s. For some OBEMs, the sampling interval was first set at 10 s and then switched to 60 s, controlled by a timer. This function helps to optimize battery power consumption more efficiently because the magnetometer is powered on intermittently for only a few seconds around the time of sampling. The 10-s sampling recordings provide shorter-period data that are sensitive to shallower parts of the oceanic lithosphere. There were also sites where the OBEMs were deployed iteratively to collect longer time series data (Table 1). The positions between these sites on the seafloor were slightly different from each other (0.4–2.0 km) because they were settled via free fall. We therefore regarded the averages as the representative positions of the sites. As addressed later, these differences in position are not critical in the analysis for study of mantle structure and topographic effects.

EFOSs measure just one component of the electric field, but with a much longer dipole (2–3 km for the NOMan experiment) than that of the OBEMs (~5.4 m), and therefore yield better signal-to-noise (S/N) ratios (Utada et al. 2013). An EFOS consists of a recorder and a cable drum attached to an anchor. The EFOS is deployed to the seafloor via free fall, and the cable drum is then caught and towed by a remotely operated underwater vehicle (ROV) *KAIKO 7000II* to extend the cable that generates the long electric dipole. An EFOS was deployed at NM03 in 2010 as the part of the pilot survey. In 2012,

the recorder was replaced and the measurements were continued. Three additional EFOSs were deployed, at NM01, NM14, and NM16. The direction of the cable extension was restricted by the recorder side because of the instrumental design and a technical reason of the ROV operation (Utada et al. 2013). All of the EFOS recorders happened to settle facing between N40°E and N170°E after free fall deployment; therefore, the cables were extended approximately in the N110°E direction (Table 1), which is subparallel to the direction of Pacific Plate motion. The EFOS recorders at sites NM01, NM14, and NM16 were retrieved using the ROV *KAIKO 7000II* in 2014, and the recorder at NM03 was retrieved using ROV *KAIKO Mk-IV* in 2015. Further information about the EFOSs is listed in Table 1.

The recovered time series data were first processed for quality control. Abnormal fluctuations, such as spikes and rectangular steps in raw time series data, were detected by eye through comparing different field components, and spikes were then linearly interpolated and steps were shifted to reduce discontinuity. The instrumental clock was compared with coordinated universal time (UTC) via global positioning system (GPS) just before deployment and after retrieval. The detected clock shift was corrected, based on the assumption that the shift accumulated linearly over time. For the OBEMs, the coordinate system was adjusted to a geographical one; the instrumental tilt was corrected using tilt angle data through Euler rotation, and the horizontal coordinate system was then rotated using the magnetic field declination predicted from the international geomagnetic reference field (IGRF) (IAGA Working Group V-MOD 2010). Coordinate system conversion was not applied to the EFOS data because the EFOSs measured only one component of the electric field.

Magnetotelluric analysis

The MT response $\mathbf{Z}(\mathbf{r}, T)$ is defined as a 2×2 complex-valued tensor transfer function between the horizontal electric $\mathbf{E}(\mathbf{r}, T)$ and magnetic $\mathbf{B}(\mathbf{r}, T)$ fields,

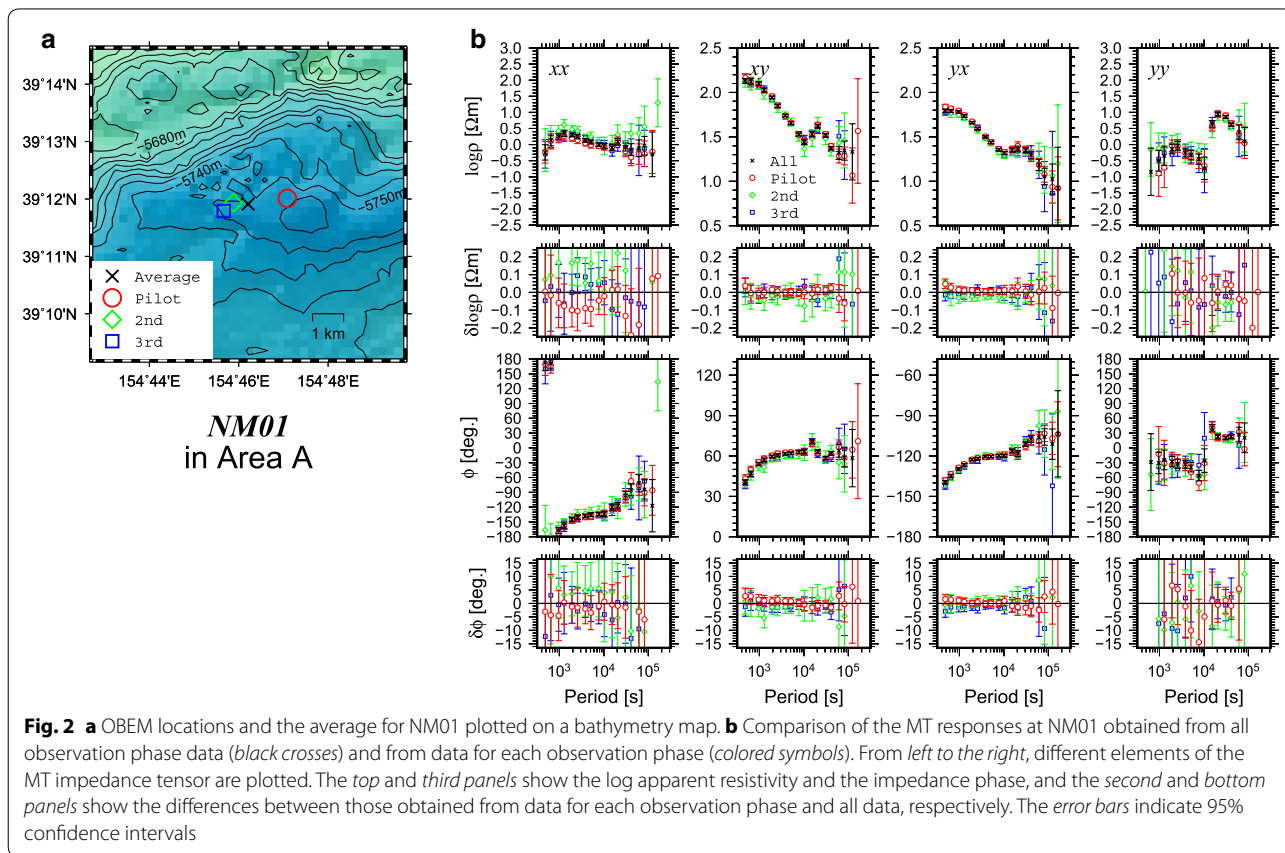
$$\mathbf{E}(\mathbf{r}, T) = \mathbf{Z}(\mathbf{r}, T)\mathbf{B}(\mathbf{r}, T), \tag{1}$$

where \mathbf{r} is the observed position and T is the period. The responses were estimated for each OBEM site using a bounded influence algorithm (Chave and Thomson 2004). The magnetic field data from the Kakioka observatory (KAK) were employed as a remote reference to reduce the effects of site-dependent noise in the local (OBEM) magnetic field data. We also applied a generalized remote reference method based on two-stage processing (Chave and Thomson 2004). In the first stage, a transfer function between the local and remote horizontal magnetic fields was estimated, and in the second stage, the MT responses were estimated as a transfer function between the local observed electric field and the local horizontal magnetic field estimates predicted from the inter-site magnetic transfer function obtained in the first stage. The generalized remote reference method significantly improved the quality of the MT response estimation for periods shorter than ~ 500 s at the sites where 10-s sampling data were available. The final responses for each period were taken from those obtained using either the normal or generalized remote reference method with higher coherence. Finally, the MT responses were obtained for the period range between 53.3 and 163,840 s

(the available range depends on the site). The longest available period is limited to 163,840 s, although data for more than 3 years were used, mainly because the S/N ratio of the electric field measured by the OBEMs becomes quite low with fluctuations over longer periods.

We examined the influence of the different positions of the OBEMs deployed in the different observation phases by comparing the MT responses estimated from data for each observation phase and from all observation phases. For NM01, data are available from three observation phases (Table 1). The distances between pairs of OBEM positions are 0.4–2.0 km (Fig. 2a). The resulting MT responses all agree within the 95% confidence interval (Fig. 2b). These results suggest that, in the present study, relocation error is not critical in this analysis of mantle structure and topographic effects. Therefore, we used the MT responses estimated from all available observation phase data to represent the response at each site and used the average position for the MT response simulation in the following analysis.

The OBEM magnetic field data and EFOS data at the same sites were also processed jointly to yield a scalar MT response between the electric field along the EFOS dipole and the OBEM magnetic field component perpendicular to the EFOS dipole. In addition, the geomagnetic depth



sounding (GDS) response, which is the transfer function between the vertical component and the horizontal component of the magnetic field, was estimated for each OBEM site and for the seafloor observatory at the North Western Pacific (NWP) (Toh et al. 2006). These responses were estimated for periods longer than $\sim 10^5$ s and are therefore useful to evaluate deeper structure. Matsuno et al. (2017) have provided a detailed analysis of the data and discussion of the structure of the mantle transition zone. Therefore, in this study, we focus on analysis of the MT responses obtained with the OBEM data and discussion of the upper mantle structure.

Examples of the MT responses representative of each area (NM01 for Area A and NM24 for Area B) are plotted in the form of apparent resistivity and impedance phase sounding curves to reveal the variation as a function of period (Fig. 3). See Additional file 1: Figure S1 for the sounding curves of all sites. In Fig. 4, polar diagrams of the apparent resistivity (Swift 1967) are plotted, as well as phase tensor ellipses (Caldwell et al. 2004), on a bathymetric map for two selected periods (640 and 5120 s) to illustrate the lateral variations of the tensor MT responses.

We first show the overall features of the sounding curves. With periods shorter than about 500 s (Fig. 3), the apparent resistivity and phase in the major elements decrease with decreasing period, which suggests that the uppermost layer is relatively conductive, likely associated with the crust including a thick (~ 400 m) pelagic sediment layer (Shinohara et al. 2008). The apparent resistivities show a peak at around 500 s and then decrease with increasing period (Fig. 3). This feature is typical for oceanic mantle that consists of cool, resistive lithosphere and underlying hotter, more conductive asthenosphere (e.g., Filloux 1977). The peak of the apparent resistivity is higher for Area B than for Area A (Fig. 3). The responses look similar between sites within each area, but the spatial variation tends to differ somewhat between Area A and Area B. For example, the phase tensors at 5120 s tend to elongate in the northeast–southwest direction in Area A, but form a more circular shape in Area B (Fig. 4). These observations suggest a difference in the upper mantle structure at a scale beyond the array size. Splitting between the off-diagonal elements suggests the effect/s of lateral heterogeneity and/or anisotropic structure. This phenomenon is smaller for Area B, which is more distant from the coastlines; therefore, the coast effect is likely a possible cause. In fact, our previous study showed that splitting in the responses for Area A is partly explained by the topography, including coastlines (Baba et al. 2013a). However, for Area A, the splitting tends to be slightly more significant at the western sites, NM01, NM02, and NM04 (Fig. 3; Additional file 1: Figure S1), and this feature is not reproduced

well with the topographic effect alone (Baba et al. 2013a), which suggests the presence of lateral heterogeneity within the array or at a slightly larger scale. At periods of about 10^4 s, both the apparent resistivities and phases, especially for the xy and yy elements, abruptly change (Fig. 3). This feature is more significant for Area B, which is the most distant from the reference site (KAK). It is likely caused by imperfect reduction of Sq effects (Shimizu et al. 2011). Therefore, we have down-weighted the responses within the period range of 10^4 – 10^5 s, where the Sq effects dominate, in later analysis. Nevertheless, the splitting between the off-diagonal elements likely decreases with increasing periods, which suggests that the deeper part of the upper mantle tends to be more uniform laterally.

Topographic effect correction and inversion

We estimated one-dimensional (1-D) isotropic electrical conductivity profiles of the mantle for Area A and Area B separately, which fit the MT response averaged in each array, by applying an iterative topographic effect correction. The 1-D profile estimated by this procedure should be a representative of average 1-D structure of possibly laterally heterogeneous (and/or anisotropic) mantle beneath each array. We do not argue that the mantle structure is one-dimensional as we discuss possible lateral heterogeneity and anisotropy later. This procedure is critical to obtain a reliable subsurface structure model because the large contrast in conductivity between seawater and crustal rocks can severely distort the EM field at the seafloor. This procedure is based on our previous studies (Baba and Chave 2005; Baba et al. 2010, 2013a, c) and consists of four steps. The procedure of these steps is iterated until the results converge to obtain the final 1-D profile, as described below.

In Step 1, we first calculate a scalar MT response from the tensor MT response at each site. We adopt the square root of the determinant of the tensor MT response, $Z_{\text{det}} = \sqrt{Z_{xx}Z_{yy} - Z_{xy}Z_{yx}}$, which is an invariant to rotation of the horizontal coordinate system, following the methods of our previous studies (Baba et al. 2010, 2013a). Rung-Arunwan et al. (2016) demonstrated that another rotational invariant based on the sum of squared elements, $Z_{\text{ssq}} = \sqrt{[Z_{xx}^2 + Z_{xy}^2 + Z_{yx}^2 + Z_{yy}^2]/2}$, is more robust to galvanic distortion. However, the distortion indicators, $\gamma = Z_{\text{ssq}}^2/Z_{\text{det}}^2$ (Rung-Arunwan et al. 2016), are real and nearly equal to unity independently of period for all sites, which indicates that Z_{det} is almost identical to Z_{ssq} (Fig. 5) and that the present dataset is affected little by galvanic distortion. This observation is consistent with the negligibly small relocation error mentioned above and can be attributed to the fact that oceanic crust generated at the mid-ocean ridge with thick sedimentary cover

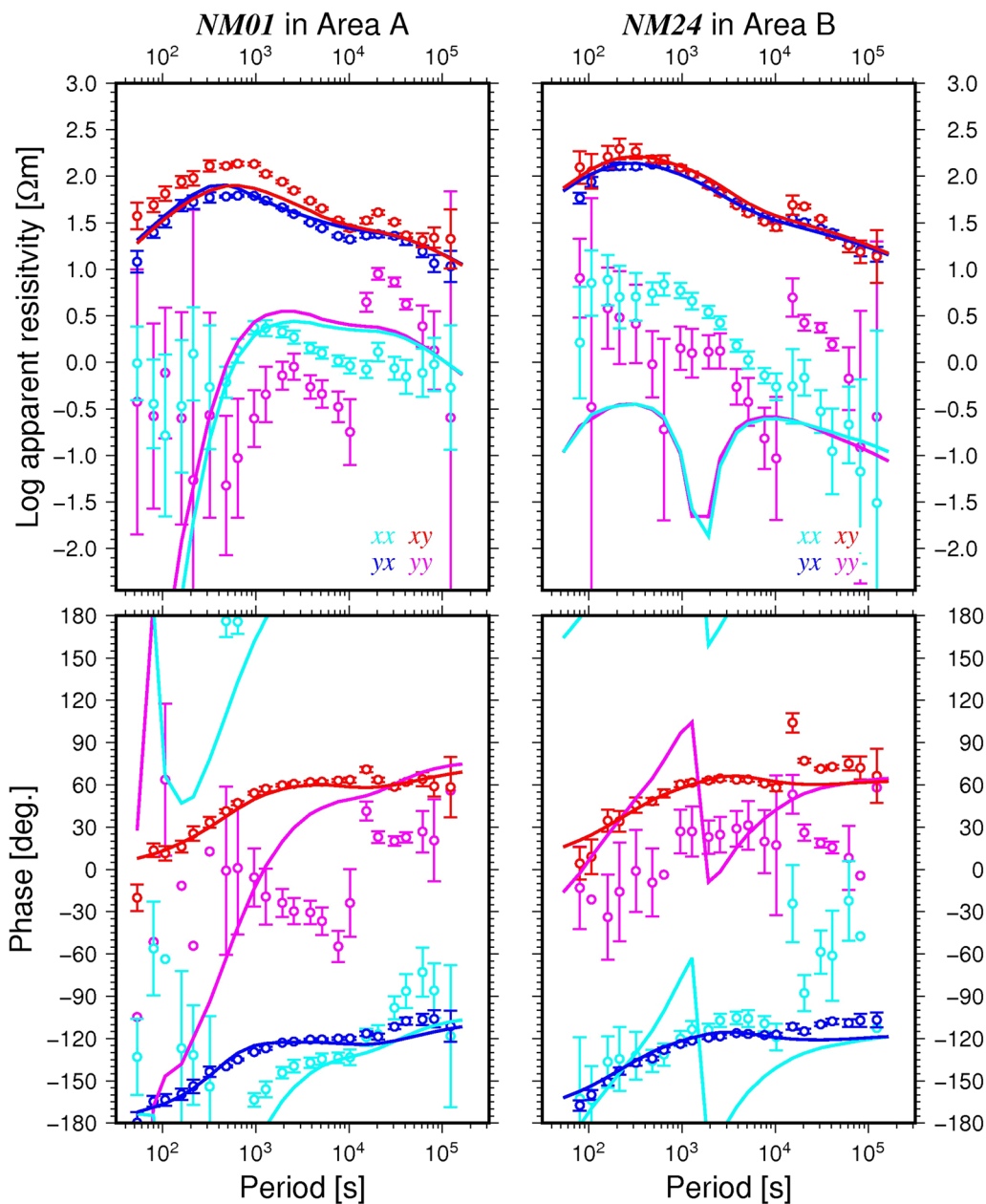
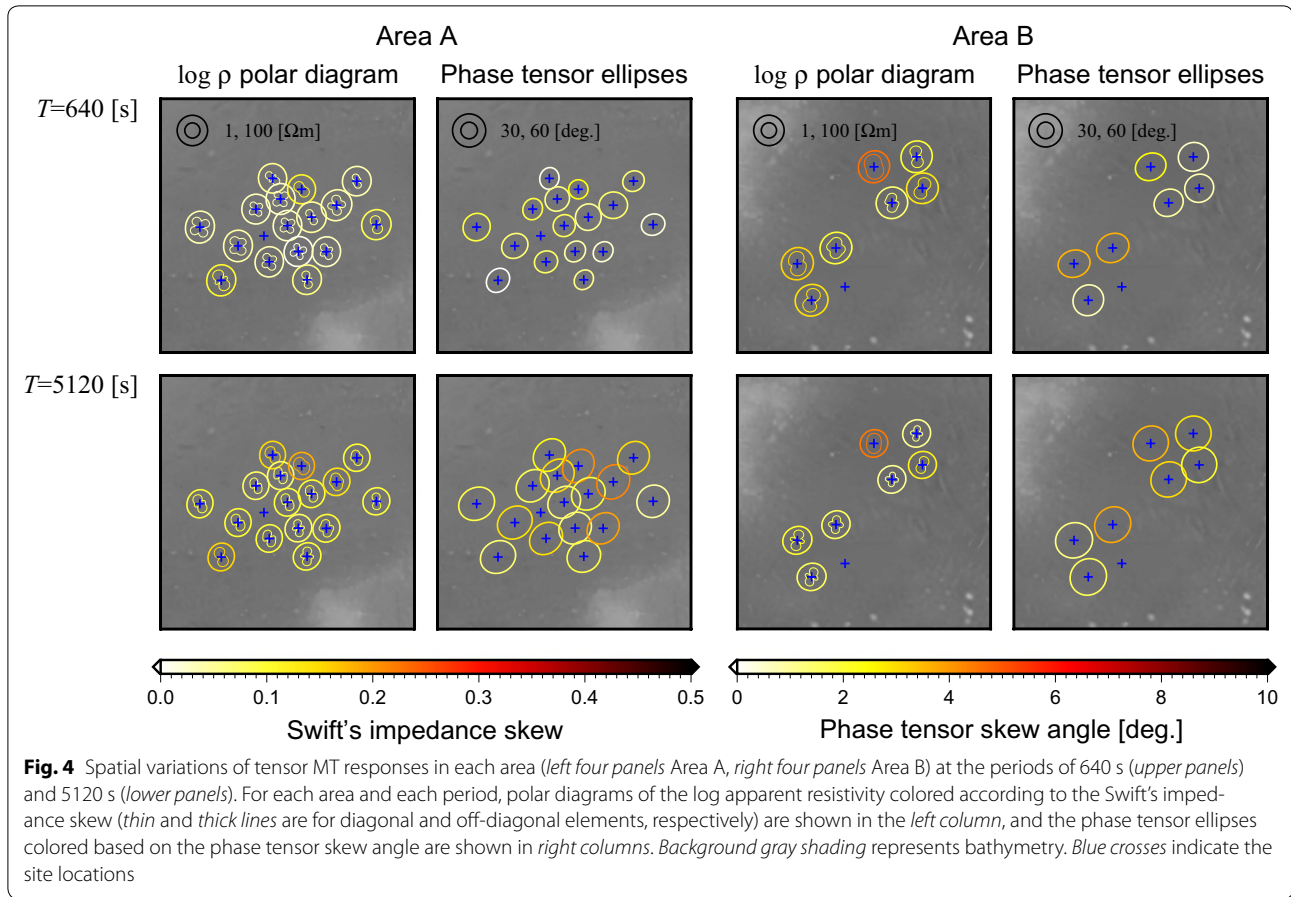


Fig. 3 Examples of MT responses for Area A (left) and Area B (right) in terms of apparent resistivity (top) and impedance phase (bottom) sounding curves; x and y represent the geographical coordinate system. Symbols with error bars are the observed responses. The error bars indicate 95% confidence intervals. Solid lines are the responses predicted from a conductivity structure model that consists of the known 3-D topography over the estimated 1-D mantle structure

is generally much more homogeneous geologically than continental crust that has undergone tectonic processes and erosions. The estimates of $Z_{det}(\mathbf{r}, T)$ for all sites are then averaged in each array for each period.

In Step 2, Occam’s inversion (Constable et al. 1987) is applied to the averaged response $\bar{Z}_{det}(T)$ to obtain a representative 1-D profile. The error floor of 2.5% of $|\bar{Z}_{det}|$ is applied, except for the periods between 10^4 and 10^5 s, to

which an error floor five times larger (12.5%) is applied, because the responses in these periods are likely distorted by imperfect reduction of Sq effects, as described above. The conductivity at ~ 30 km depth is constrained to be $10^{-3.5}$ S m^{-1} in the inversion, following our previous studies (Baba et al. 2010, 2013a), because the inversion of \bar{Z}_{det} with the smoothness constraint does not always reproduce such a resistive layer, although there is



no doubt that the cold lithosphere exhibits very low conductivity (e.g., Baba et al. 2010, 2013a; Cox et al. 1986). The inversion did not converge if the target misfit was set to 1.0. Then, the target misfit was set to 1.24 and 1.25 for Area A and Area B, respectively, which correspond to the 99% confidence limit of χ^2 misfit. The uncertainty of the conductivity of each layer is estimated by evaluating the distribution of the acceptable models obtained through numerous inversion runs with different constraints, following our previous studies (Baba et al. 2010, 2013a).

In Step 3, the topographic effect is simulated. A two-stage three-dimensional (3-D) forward modeling approach (Baba et al. 2013c) is applied to incorporate the effects of regional large-scale topography and local small-scale topography. The lateral dimensions of the regional model are 10,000 km \times 10,000 km, and the horizontal mesh in the central area that includes the array is 50 km \times 50 km. The local model is as large as 350 km \times 350 km, with topography in the vicinity of each site based on MBES data and is also incorporated with a finer mesh (1 km \times 1 km in the central area) in the second stage forward modeling (Baba et al. 2013c). Figure 6a

shows the regional topography models for the two areas, and Fig. 6b shows examples of the local topography model at a particular site for each array. The regional model includes the East Asian coastlines and major topographic features such as abyssal rises and trenches. The local models incorporate finer-scale topographic changes, such as linear hills and valleys subparallel to the past seafloor spreading ridge. The conductivity values of seawater and land crust are set to 3.2 and 0.01 S m⁻¹, respectively. The 1-D profile obtained in Step 2 is incorporated in the subsurface structure.

In Step 4, the topographic distortion terms for each site, $\mathbf{D}(\mathbf{r}, T)$, are calculated from the 3-D and 1-D forward responses $\mathbf{Z}_{3-D}^{\text{pre}}(\mathbf{r}, T)$ and $\mathbf{Z}_{1-D}^{\text{pre}}(T)$, assuming that the 3-D response to be observed is expressed by multiplication of the surface 3-D topographic distortion and the response to the subsurface 1-D structure,

$$\mathbf{D} = \mathbf{Z}_{3-D}^{\text{pre}} (\mathbf{Z}_{1-D}^{\text{pre}})^{-1}. \quad (2)$$

Then, the observed responses $\mathbf{Z}^{\text{obs}}(\mathbf{r}, T)$ are corrected as,

$$\mathbf{Z}^{\text{cor}} = \mathbf{D}^{-1} \mathbf{Z}^{\text{obs}}. \quad (3)$$

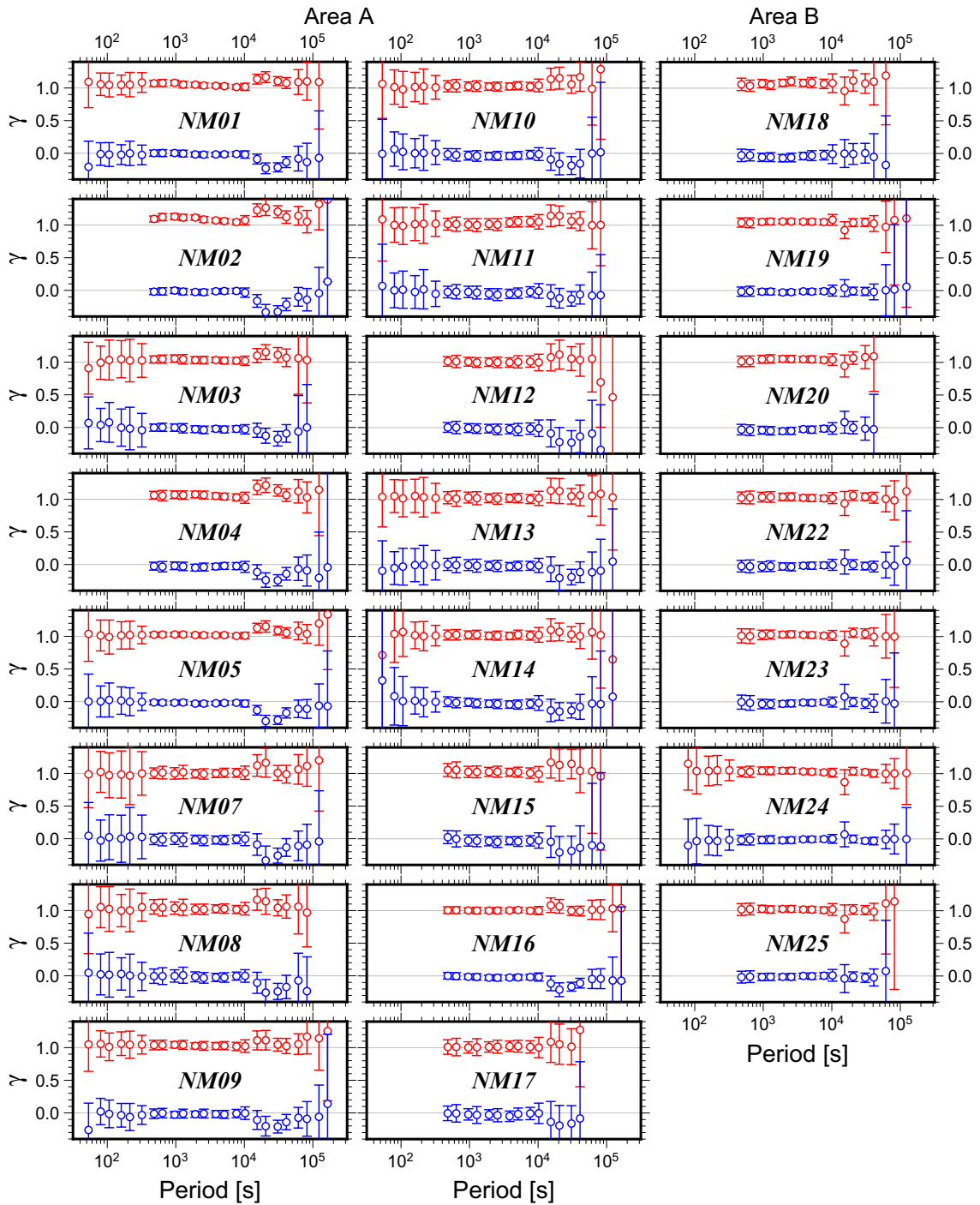


Fig. 5 Local distortion indicators (Rung-Arunwan et al. 2016) for all sites in Area A and Area B. Red and blue symbols denote the real and imaginary parts, respectively. Error bars are 95% confidence limits

We evaluate the root mean squared (RMS) misfit between the observed (non-corrected) and predicted responses in terms of log apparent resistivity $\log \rho$ and impedance phase ϕ ,

$$RMS = \sqrt{\frac{1}{2N_d} \sum_{i=1}^{N_d} \left[\left(\frac{\log \rho_i^{obs} - \log \rho_i^{pre}}{\delta \log \rho_i} \right)^2 + \left(\frac{\phi_i^{obs} - \phi_i^{pre}}{\delta \phi_i} \right)^2 \right]}, \tag{4}$$

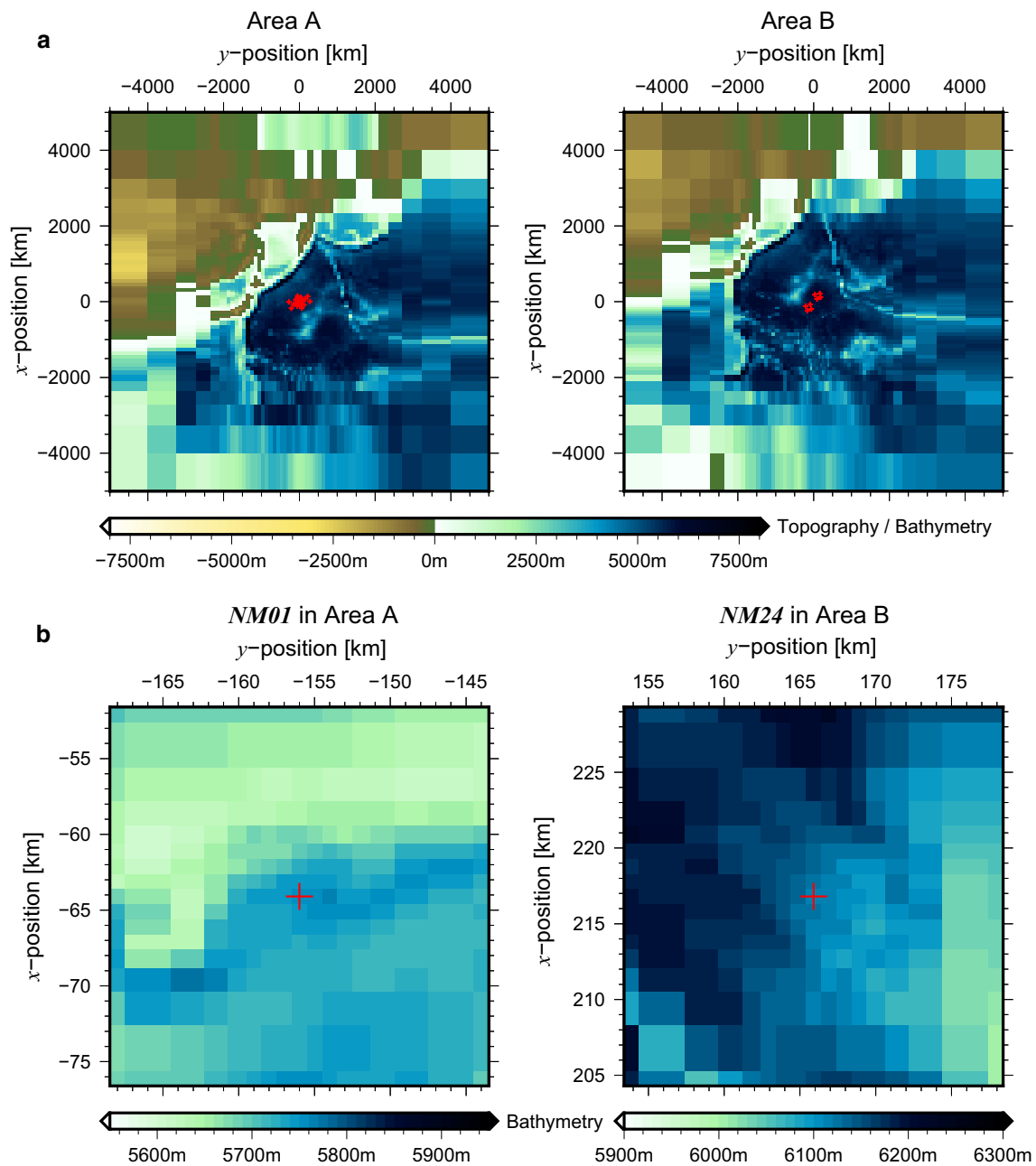


Fig. 6 **a** Regional topography models for Area A and Area B. **b** Example local topography models for NM01 in Area A and NM24 in Area B (only the central area of the model is plotted to show small-scale topography)

where N_d is the total number of data points for \mathbf{Z} involving four elements of the tensor, the number of available periods, which depends on the site, and the number of sites. The parameters $\delta \log \rho$ and $\delta \phi$ are the standard errors, to which the error floor is applied. Error floors are set to 2.5% for the off-diagonal elements of \mathbf{Z} , for the diagonal elements, are set to the absolute value of 0.01 for periods

shorter than 3000 s, and 5.0% for the longer periods. These criteria are based on our experience regarding the approximate accuracy of regional 3-D forward modeling. However, for periods between 10^4 and 10^5 s, the error floors are increased by a factor of five, i.e., to 12.5 and 25.0% for off-diagonal and diagonal elements, respectively, for the same reason as for the 1-D inversion in Step 2.

Results

Figure 7a presents $Z_{\text{det}}(\mathbf{r}, T)$ and $\bar{Z}_{\text{det}}(T)$ from Area A and Area B, as obtained in Step 1. The averaged responses differ significantly between the two areas, and this difference is beyond the dispersion between sites within each area. These features remain after topographic effect correction (Fig. 7c), which suggests that the subsurface structures differ significantly between the areas. The topographic effect correction increased the apparent resistivity at longer periods for both areas, but the change is larger for Area A than for Area B. Therefore, this change should mainly be attributed to relatively large-scale topographic effects, such as the coastlines west of the study areas. The dispersions in the responses within each array, which are larger with shorter periods, changed little with topographic effect correction. This result indicates that local topographic effects, which should affect the responses in shorter periods more strongly, are not as significant as the regional topographic effects and

that the dispersions are caused by lateral heterogeneity in subsurface (but relatively shallow) structure. Because the dispersion is very small within Area B, the subsurface structure beneath Area B is inferred to be more uniform laterally.

The topographic effect correction and inversion procedure was iterated twice. Changes in RMS misfit against the iterations are listed in Table 2. Figure 8 shows the residuals between the responses observed and predicted from the final model, which were normalized based on the relative errors $\delta Z/|Z|$ after applying the error floors. The errors for each element are of a similar level for the two areas, such that the difference in the RMS misfit approximately reflects the difference in the absolute model fit. The RMS misfit decreased significantly at the first iteration and then slightly increased again at the second iteration; therefore, we took the result at the first iteration as the final model. The reduction of the misfit from the initial to the final model is as small as 14% for

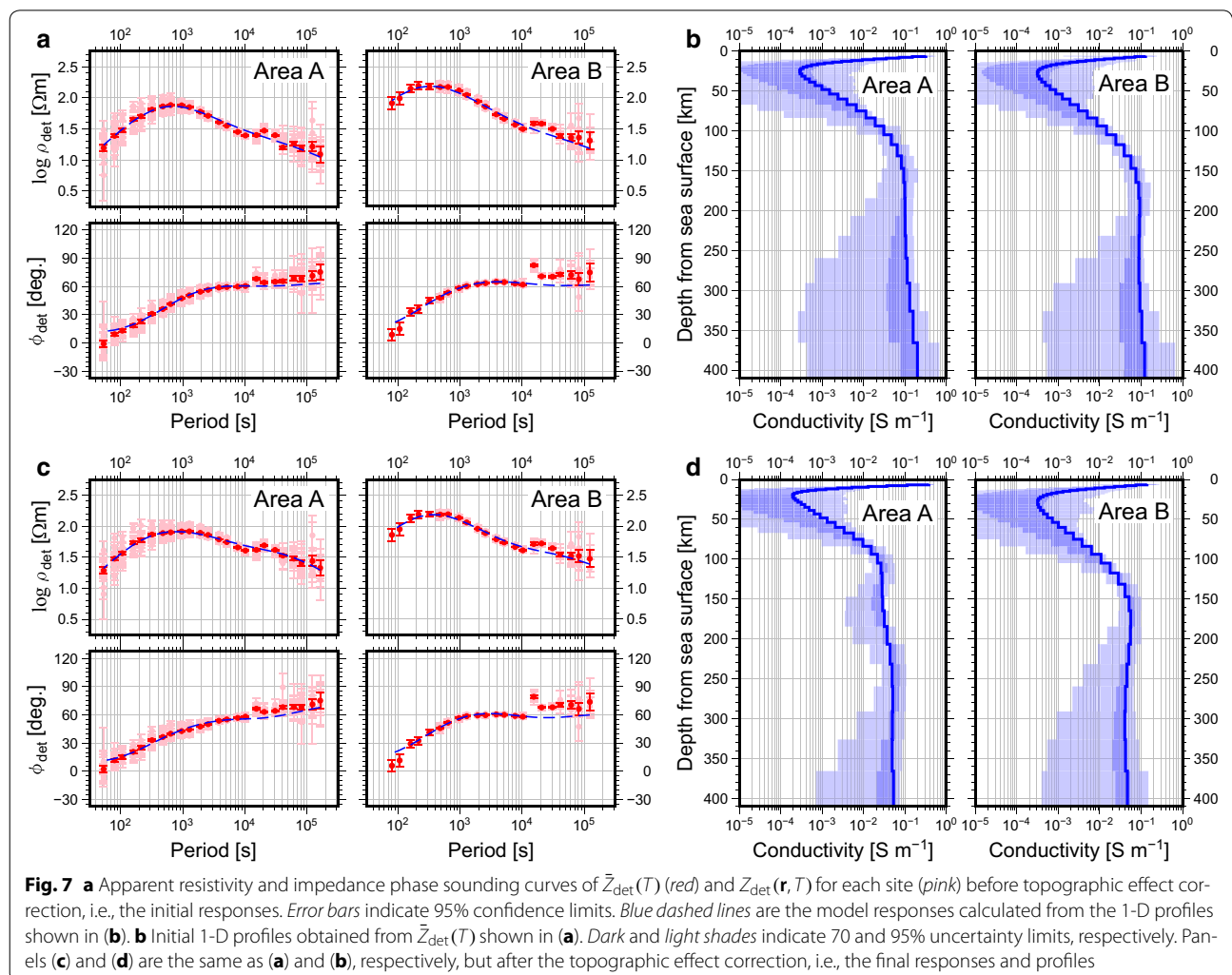


Table 2 The RMS misfit against the iteration

Iteration	Area A					Area B				
	Total	xx	xy	yx	yy	Total	xx	xy	yx	yy
0	4.66	5.40	4.86	3.02	4.98	9.32	17.51	2.35	3.03	5.16
1	3.99	4.80	3.19	2.54	4.92	9.10	17.28	2.15	1.88	4.94
2	4.08	5.05	2.79	3.01	4.92	9.12	17.31	2.15	1.89	4.97

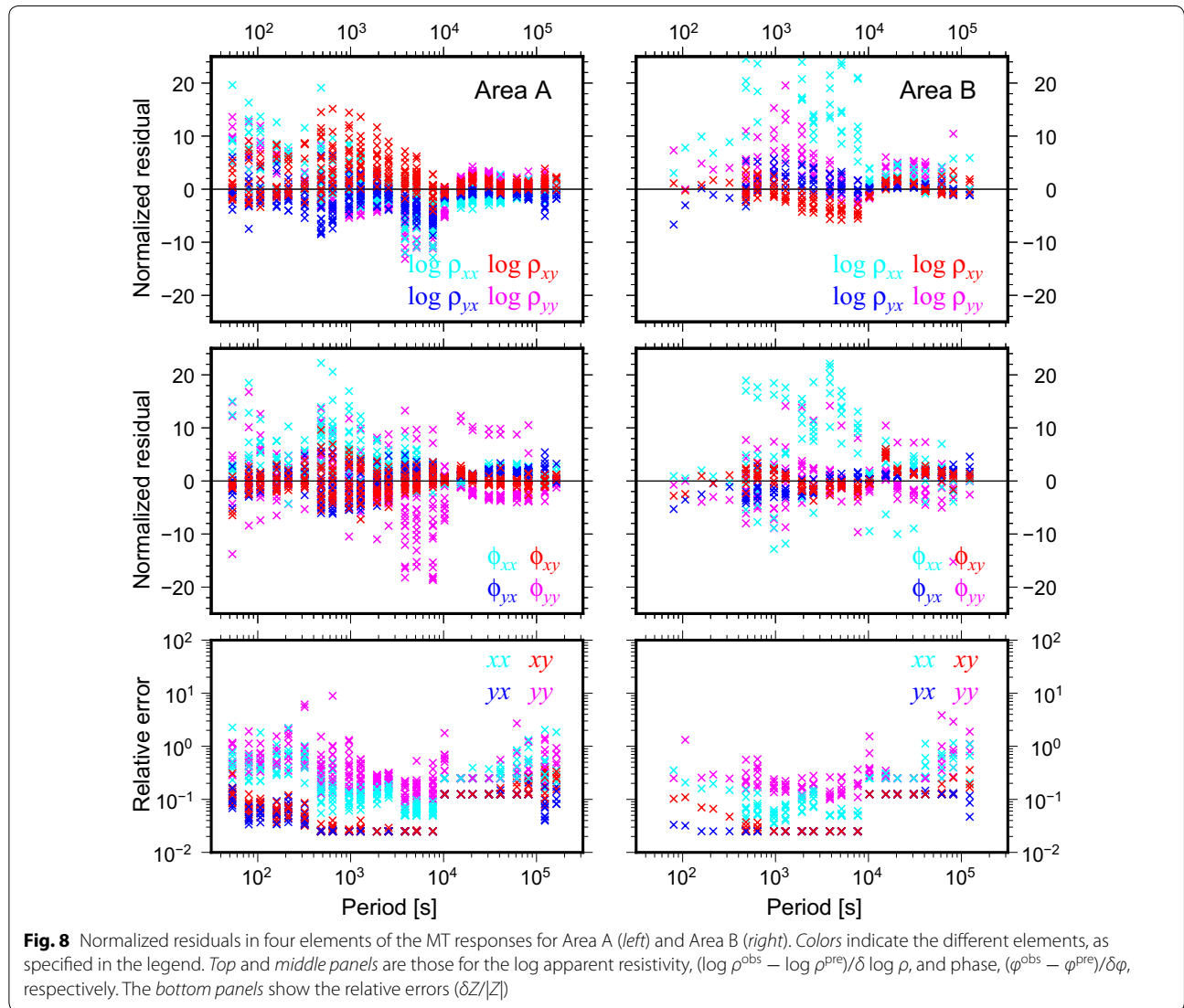


Fig. 8 Normalized residuals in four elements of the MT responses for Area A (left) and Area B (right). Colors indicate the different elements, as specified in the legend. Top and middle panels are those for the log apparent resistivity, $(\log \rho^{\text{obs}} - \log \rho^{\text{pre}}) / \delta \log \rho$, and phase, $(\varphi^{\text{obs}} - \varphi^{\text{pre}}) / \delta \varphi$, respectively. The bottom panels show the relative errors $(\delta Z / |Z|)$

Area A and 2% for Area B. This small reduction indicates that the initial 1-D models were good enough compared to other choices for the initial model, such as a uniform half space, which is frequently used for inversion analyses (Baba et al. 2013a). For Area B, the RMS misfit is almost twice of that for Area A, and the reduction was smaller. This difference occurs because for Area B, the RMS misfit

of the *xx* element is extremely high compared to that for the off-diagonal elements (Table 2; Fig. 8). The partial RMS misfits for the off-diagonal elements for Area B were smaller than those for Area A, and the reductions were as large as 9–38%.

The predicted responses explain the overall features of the observed responses, although there are some

significant differences between them (Figs. 3, 8). Relatively large misfits are mainly seen with periods shorter than several thousand seconds. For Area A, the splitting between the xy and yx (off-diagonal) elements or the xx and yy (diagonal) elements of calculated responses is smaller than the observed splitting (Fig. 3; Additional file 1: Figure S1), as was pointed out in our previous study based on the pilot survey data (Baba et al. 2013a). For Area B, in contrast, the off-diagonal elements are very well reconstructed by the model. However, as shown in Fig. 3, the predicted apparent resistivities for the two diagonal elements are similar and much smaller than the observed values. They are largely depressed and accompanied by a large phase change at ~ 2000 s. In addition, the observed apparent resistivity for the xx element is higher, and its errors are smaller than those for the yy element. These values resulted in the high partial RMS misfit for the xx element (Fig. 8; Table 2). These features cannot be reproduced by the topographic effect alone and therefore must be attributed to lateral heterogeneity and/or anisotropy of the subsurface structure. We expect future studies to better explain these features.

The 1-D profiles before and after the topographic effect correction for each area are shown in Fig. 7b, d. As anticipated from the observed sounding curves, the profiles were characterized by three layers, consisting of the uppermost conductive layer, the resistive lithospheric mantle, and the conductive asthenospheric mantle. As a result of topographic effect correction, the conductivity of the asthenospheric mantle decreased from the initial profile to the final profile. This reduction is more

significant for Area A. Major differences in the final profiles between the two areas are: (1) the thickness of the resistive layer and (2) the conductivity values at the peak in the upper mantle. The definition of the thickness of the resistive layer is somewhat ambiguous because the profiles change smoothly with depth, and the gradient is controlled by the smoothness constraint in the inversion as well as by the data. If we define this thickness as the depth where the conductivity become greater than 0.01 S m^{-1} , that thickness is ~ 90 km for Area A and ~ 100 km for Area B. It is quantitatively certain that the resistive layer in Area A is thinner than that in Area B. In the highly conductive zone below the resistive layer, the depth-dependent trend is much more gradual, with values of $0.02\text{--}0.03 \text{ S m}^{-1}$ at depths of 100–150 km in Area A, and $\sim 0.05 \text{ S m}^{-1}$ at depths of 150–200 km in Area B.

Discussion

Update of the model for Area A

The number of available sites for Area A was increased from four in the previous study (Baba et al. 2013a) to 16 in this study with completion of the main observation phase. The variation of observed MT responses in the array is of a similar level with that of the pilot survey array (four western sites). The obtained 1-D profile for mantle depth is also similar to the previous profile, which indicates that extension of the data to include shorter periods in this study did not affect the evaluation of the mantle, as is our main target. However, significant improvement is apparent in the uncertainty for the shallowest part of the profile (Fig. 9), which indicates that the

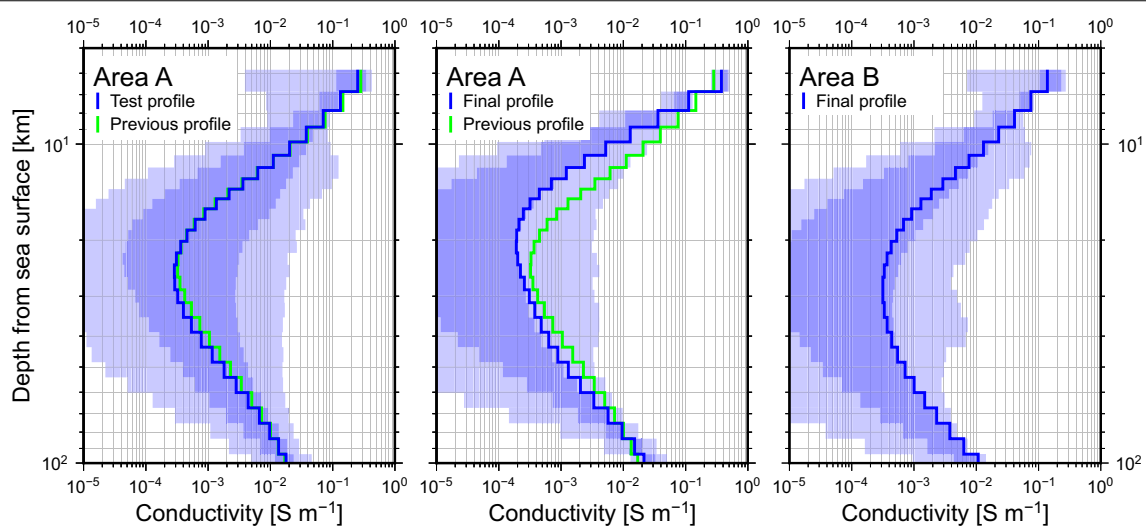


Fig. 9 Shallower part of the 1-D profiles with uncertainties. Note that the depth in the vertical axis is given in log scale for clarity. *Left* the test profile for Area A; the data for the shorter three periods were excluded in the inversion. *Middle and right* the final profiles for Area A and Area B, respectively, which are identical to those in Fig. 7d. *Green line* represents the profile obtained from the pilot survey data in Area A in the previous study (Baba et al. 2013a)

conductive oceanic crust is better constrained by the new data and thus that the conductivity values are more reliable. We ran an inversion for a test with the present data but excluded some data points at periods shorter than 160 s, as in the previous study. The resulting profile is very similar to the previous one, but the uncertainty of the final profile in this study is much smaller.

This improvement enables us to probe the uppermost mantle and crust (down to ~ 10 km below the seafloor) more reliably, even at the deep seafloor. The uppermost layer for Area A seems to be more conductive than those for Area B, although the uncertainty for Area B is larger than that for Area A (Fig. 9). Shinohara et al. (2008) conducted a seismic survey in the eastern end of our array in Area A and showed that the sediment layer is as thick as ~ 400 m. The seismic survey by Ohira et al. (2017) along a line 150 km southeast of our array in Area B showed that the thickness of the sediment layer is ~ 300 m. Both studies reported similar characters; the P-wave velocity structure in the crust below the sediment indicated typical oceanic crust, except for the transitional layer from the crust to the mantle. Although our models do not resolve the shallowest layer, which is thinner than 1 km, the thin but very conductive sediment layer can influence the mean conductivity in the uppermost layer in the inversion. Therefore, the difference between the shallower parts of the profiles from the two areas may be ascribed to the difference in the thickness of the sediment layer.

Possibilities of lateral heterogeneity and anisotropy within each area

The MT responses show some degree of spatial variations within each array (Figs. 4, 7a, c), which suggests the presence of lateral heterogeneity and/or anisotropy in conductivity. Although detailed 3-D and anisotropy analyses are now underway in subsequent studies, here we argue some implications regarding the lateral heterogeneity and anisotropy in the upper mantle for each area. Figure 10 shows the spatial distribution of the residuals between the apparent resistivity of $Z_{\text{det}}(\mathbf{r}, T)$ after the topographic effect correction and the forward response to the final 1-D profiles for each area. At three selected periods, 1280, 2560, and 5120 s, the apparent resistivity decreases with increasing period for both Area A and Area B, which suggests that the data for these periods may be responsible for the depths from the base of resistive layer to the underlying conductive zone. The radii of the colored circles in the figure are normalized for the standard error of the log apparent resistivity to demonstrate that the residuals with larger circles are more reliable than those with smaller circles. For Area A, the spatial trend is not very clear at 1280 s, but the eastern sites are more conductive at longer periods. For Area

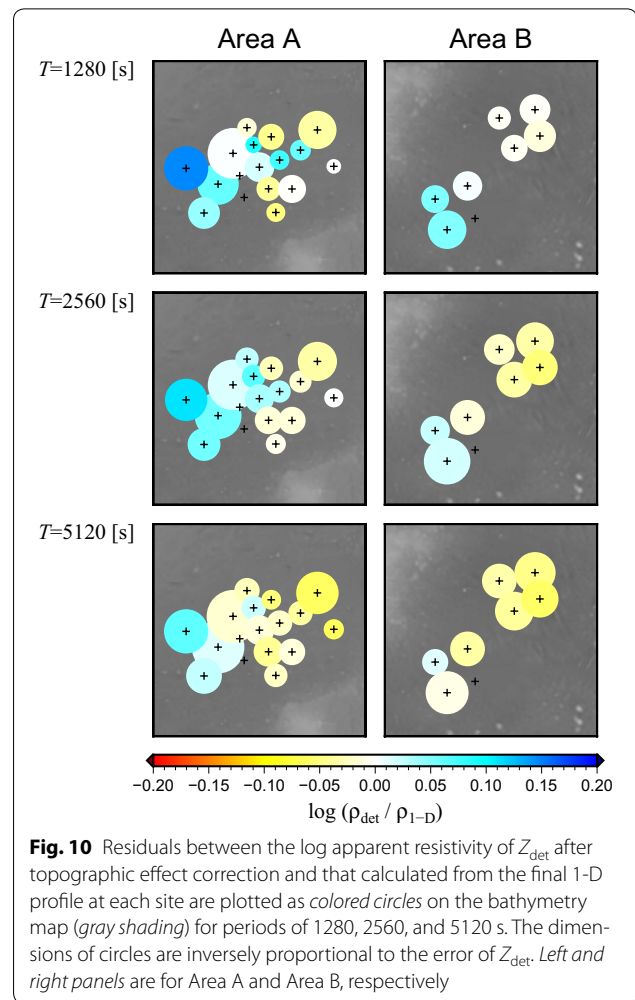


Fig. 10 Residuals between the log apparent resistivity of Z_{det} after topographic effect correction and that calculated from the final 1-D profile at each site are plotted as colored circles on the bathymetry map (gray shading) for periods of 1280, 2560, and 5120 s. The dimensions of circles are inversely proportional to the error of Z_{det} . Left and right panels are for Area A and Area B, respectively

B, the northeastern region tends to be more conductive with all three periods, although the spatial variation is smaller than that in Area A. The overall difference in the data between Area A and Area B is significantly larger than the dispersion of the data within each array (Figs. 7, 10). Therefore, the major difference in the 1-D profiles between the two areas is a robust feature.

Anisotropy in the lithosphere and asthenosphere is an important property to assess mantle dynamics, although observational evidence is available only from relatively young oceanic mantle in the eastern Pacific region (Evans et al. 2005; Baba et al. 2006a, b; Naif et al. 2013). Recent experimental studies have also demonstrated that hydrous olivine and partially molten rock can be highly anisotropic under the temperature and pressure conditions of the asthenosphere (e.g., Dai and Karato 2014; Zhang et al. 2014; Pommier et al. 2015). Therefore, the possibility of anisotropy should not be ruled out for the old oceanic mantle in our study areas. Qualitatively, we can infer that the anisotropy in the study areas, if it

exists, may be weaker than that observed in the southern East Pacific Rise (Evans et al. 2005; Baba et al. 2006a, b) because the major (off-diagonal) elements of the observed MT responses show only slight variation with rotation in horizontal coordinates (Fig. 4). Therefore, special care is necessary in examining the existence and degree of anisotropy more quantitatively, because the present MT data are affected by the 3-D topography, and mutual coupling between the topographic effect and the anisotropic mantle structure must be considered. Such a careful study is currently in progress to explore how the topography and possible anisotropy affect MT responses. Details of this analysis and its results will be reported elsewhere.

Spatial dependence of electrical conductivity of the upper mantle in the northwestern Pacific and its implication for the lithosphere–asthenosphere system

The electrical conductivity of the upper mantle differs between Area A and Area B, as demonstrated in the previous section. The major differences in the upper mantle are the thickness of the resistive layer and the high conductivity beneath the resistive layers. We confirmed that these differences are significant and not artifacts because of the high conductivity at the uppermost layers, through synthetic inversion tests (see Additional file 2: Figure S2). The seismological observations of the NOMan project have also revealed noticeable differences in shear-wave velocity structure between the two areas through surface wave tomography. The upper high-velocity layer tends to be thicker for Area B than for Area A, and the underlying low-velocity zone tends to show slower velocities for Area A than for Area B (Isse et al. 2017). The electrical conductivity and seismic slowness in the upper mantle can both be enhanced primarily by temperature increase. Therefore, the trends in the thickness of the upper resistive layer and the high-velocity layer between the two areas are qualitatively consistent, as the cool lithospheric mantle is thinner for Area A than for Area B. However, the conductivity and the velocity in the underlying conductive and low-velocity zone beneath the two areas appear to be opposite what would be explained by the thermal effect alone. This apparent inconsistency strongly suggests that other factors, such as volatile content and/or degrees of partial melting, differ in the mantle beneath the two areas. This observation also highlights the importance of further joint interpretation of seismic and EM results.

We next evaluate the spatial dependence of electrical conductivity across a wider region by comparing the 1-D electrical conductivity profiles for four areas of the northwestern Pacific. Two additional areas, Area C and Area D, are in the Pacific basin off the Bonin Trench

(the representative crustal age is ~ 147 Ma) and off the Japan Trench (~ 135 Ma), respectively (locations shown in Fig. 1), where seafloor MT data were collected in past experiments (Baba et al. 2010, 2013b). The representative 1-D profiles for Area C and Area D were previously obtained following a similar procedure to that used in the present study, but they were re-estimated in this study using the same up-to-date procedure as that applied for Area A and Area B to avoid potential artifacts due to slight differences in procedure. However, differences from the previous profiles are negligible.

Figure 11 shows the 1-D profiles for the four areas, which further highlight the variation in resistive layer thickness (the profiles in machine-readable format are given in Additional file 3: Table and the sounding curves for $\bar{Z}_{\text{det}}(T)$ (red) and $Z_{\text{det}}(\mathbf{r}, T)$ for all sites in the four areas are shown in Additional file 4: Figure S3). Area C shows the thickest resistive layer, which was also confirmed to be a robust feature by 3-D inversion analysis (Tada et al. 2014), and that of Area D falls between those of Area B and Area C. All four models differ significantly from each other. The conductivity values of the underlying high conductive zones for Area C and Area D are around $0.04\text{--}0.05$ S m^{-1} , which is close to that of Area A. That of Area B is slightly more conductive than the others.

The differences in resistive layer thickness between these four areas cannot be explained by the temperature differences of the corresponding lithospheric ages under a framework of the cooling of homogeneous mantle through thermal conduction. We have already argued this point based on the comparison of the earlier profiles for Area A and Area C (Baba et al. 2013a), and this comparison of four areas further strengthens this interpretation. Baba et al. (2013a) argued that if the mantle beneath Area A is “normal,” as expected from the plate cooling model, the lithosphere beneath Area C is abnormally thick. However, adding Area B and Area D to this comparison demonstrates that the resistive layer beneath Area A is the thinnest, and therefore represents the opposite end-member rather than the average among the four areas explored thus far. It is now more doubtful that Area A represents “normal” mantle in the old northwestern Pacific.

To demonstrate these inferences more clearly, we simulated the 1-D electrical conductivity profiles for several thermal structure models with the representative lithospheric age for each area and plotted these profiles in Fig. 11 (dashed lines). We applied simple 1-D cooling of a homogeneous, thermally conductive plate, assuming a potential temperature of 1350 °C and thermal diffusivity of 30 km² Myr⁻¹ (Turcotte and Schubert 2002). The plate thickness h is varied between 80 and 300 km. An

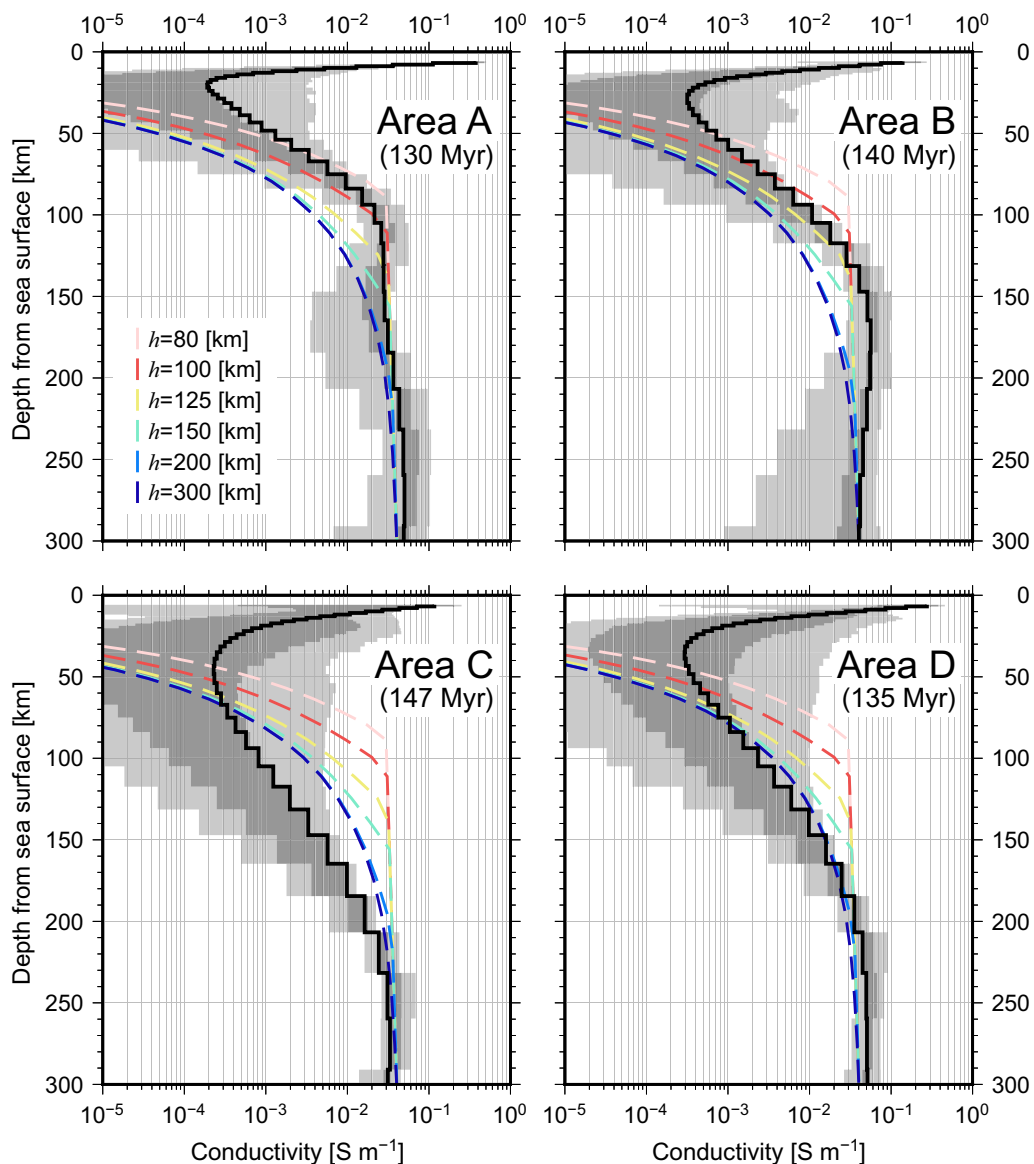


Fig. 11 Comparison of the 1-D electrical conductivity profiles for the mantle beneath four areas in the northwestern Pacific (Fig. 1). *Solid lines* are the profiles obtained through inversion. *Dark and light shades* indicate 70 and 95% uncertainty limits, respectively. *Colored, dashed lines* indicate the simulated profiles for the representative ages in each area, assuming different thicknesses of the thermally conductive plate, h (see text for details)

adiabatic temperature gradient of $0.3 \text{ }^\circ\text{C km}^{-1}$ was superimposed onto this thermal profile. The mantle electrical conductivity was assumed to be represented by that of olivine. We applied the electrical conductivity model for olivine by Gardés et al. (2014), which was obtained by compiling published experimental results. The water content dissolved in olivine was assumed to be 0.01 wt.%, which is thought to be a typical value for mid-ocean ridge basalt (MORB) source mantle (Hirschmann 2010). Note that there are two competing groups that show significantly different results for the conductivity measurement

of hydrous olivine, and therefore, selection of the laboratory model leads different impacts of water on the conductivity simulation. Olivine conductivity calculated using the model of Gardés et al. (2014) falls in a middle ground between values those calculated using the models of the two competing groups (Wang et al. 2006; Yoshino et al. 2009) in a case for water content of 0.01 wt.% at $1200 \text{ }^\circ\text{C}$ (see their Fig. 1). In the simulation, we considered only the solid-state mantle and the effects of temperature and water on that mantle. However, we do not rule out the possible contribution of partial melting due

to the presence of water and carbon dioxide (e.g., Sifré et al. 2014).

The calculated electrical conductivity profiles for any h are almost identical between the four different representative ages, because the thermal structure is almost identical in the range of ages compared here. However, the results for different values of h showed significantly different conductivity profiles. The inversion profile for Area A falls between the simulated profiles for h of 80 and 100 km. For Area B, the inversion profile is in between the profiles for h of 100 and 125 km. For Area D, it mostly corresponds to the simulated profiles for h of 200 and 300 km, which are almost the same. The resistive layer for Area C is much thicker than the simulated profile for h of 300 km, which suggests that it is more consistent with a cooling half space rather than a cooling plate, as discussed in previous studies (Baba et al. 2010, 2013a). This result suggests that the transition from the resistive to high-conductivity zones is mainly controlled by h . It is impossible to represent the 1-D profiles for all areas by a thermal model with a single value of h . In other words, it is likely that the thickness of the cool thermal lithosphere differs between these areas. If the appropriate values of h are chosen, the simulated profiles with the same value of potential temperature fit the high-conductivity zone well for all areas, although the inversion profile for Area B is slightly higher than the simulated profile at depths between 150 and 200 km. This observation suggests that the asthenospheric mantle in this region is rather homogeneous in potential temperature and chemical composition, except for Area B.

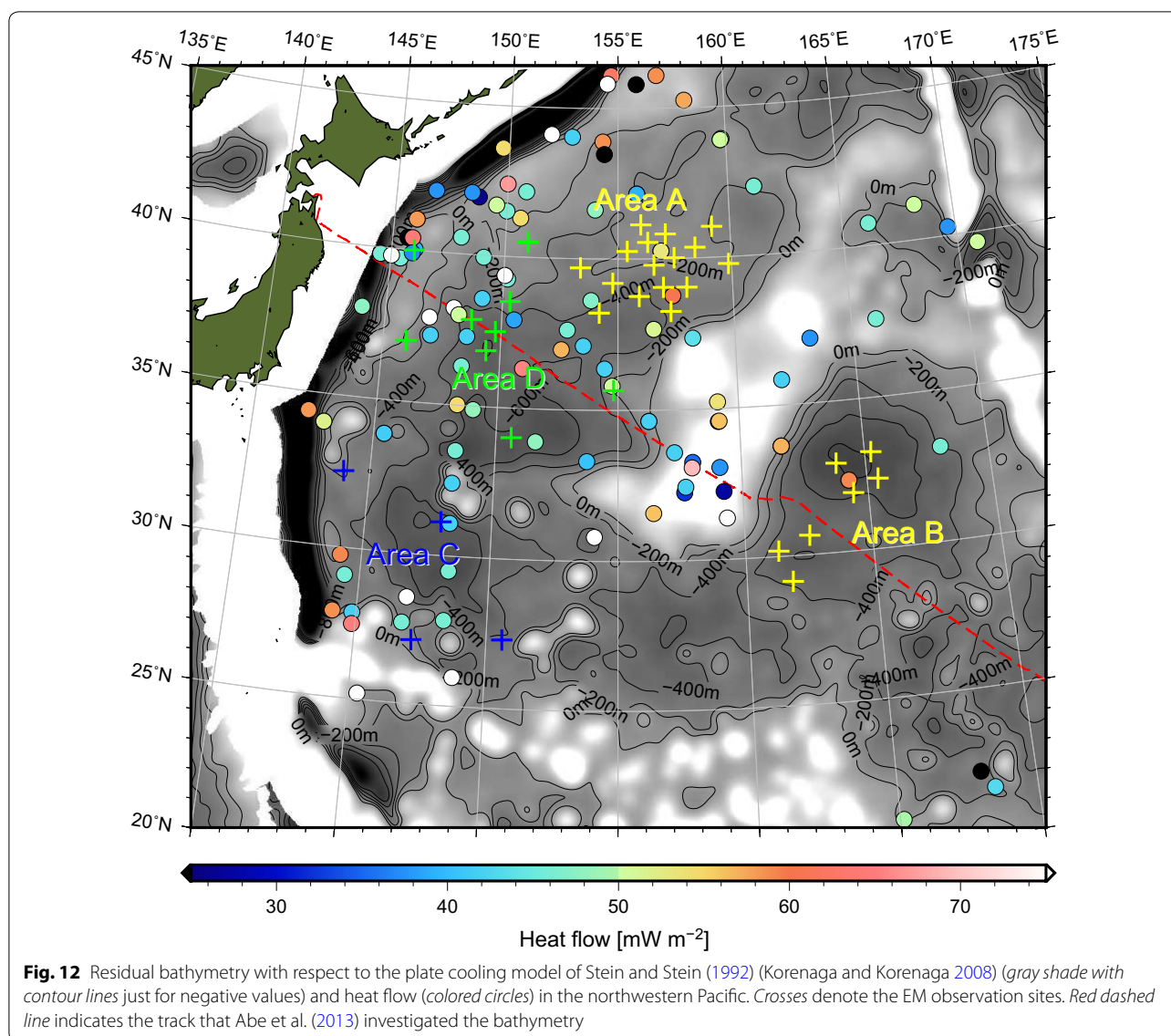
Bathymetry subsidence and heat flow data seem to be consistent partly but not perfectly with the significant trend in the resistive layer thickness between the four areas. Residual bathymetry with respect to the plate cooling model of GDH1 (Stein and Stein 1992) estimated by Korenaga and Korenaga (2008) shows that the subsidence in Area A is the most comparable (~ -200 m) with the model prediction and the other three areas are ~ 500 m deeper than the model prediction (Fig. 12). Abe et al. (2013) compared the bathymetry observed along a track crossing over Area B and Area D with the predictions by two plate cooling models, PSM (Parsons and Sclater 1977) and GDH1. Their result indicates that the seafloor in the two areas is more comparable with the prediction from PSM, which gives cooler (1350 °C) potential temperature and thicker (125 km) thermally conductive plate than that from GDH1 (1450 °C and 90 km, respectively). The bathymetry data support relatively thin thermal plate beneath Area A but do not show clear difference between the other three areas. Area C is not as deep as the prediction from a half space cooling model, which is ~ 1000 m deeper than the prediction from GDH1 (see Figure 1 of

Stein and Stein 1992). Heat flow observations are limited in the northwestern Pacific basin. For Area A and Area B, although only a few data points are available, the heat flow values are $50\text{--}60$ mW m^{-2} , which are comparable with the prediction from GDH1, while, for Area C and Area D where more data points exist, the majority show $40\text{--}50$ mW m^{-2} , which are comparable with the prediction from PSM (Fig. 12). Note that the predictions of heat flow values from a half space cooling model and PSM are not significantly different and they both are about 10 mW m^{-2} lower than the prediction from GDH1 (see Figure 1 of Stein and Stein 1992). Thus, heat flow seems to support relatively thicker (may be as thick as the half space cooling model) thermal plate beneath Area C and Area D. In summary, both bathymetry and heat flow observations suggest that it is difficult to explain all data by a unique cooling model.

It is therefore necessary to introduce more dynamic processes to explain the variation in the electrical structure beneath the northwestern Pacific, although it is still difficult to provide a reasonable and comprehensive interpretation involving all observed features. The concept of the thermally conductive plate with a finite thickness was originally introduced to explain the decrease in seafloor subsidence rate in regions older than $\sim 70\text{--}80$ Ma (e.g., Parsons and Sclater 1977; Stein and Stein 1992). However, there is no physical requirement that the temperature is constant at a certain depth over time. The concept, therefore, can be interpreted as an apparent feature of the actual thermal structure, with additional dynamic geophysical or geological processes, such as small-scale convection (e.g., Richter 1973) and/or rejuvenation by randomly distributed reheating events (e.g., Smith and Sandwell 1997), superimposed onto the cooling of a half space with thermal conduction. The difference in the electrical structures between the four areas may suggest that such a dynamic process developed with locality, or that different dynamic processes developed locally in each area.

The electrical structures, their locations, and the major tectonic features in the northwestern Pacific are graphically summarized in Fig. 13. There is a major trend in the thickness of the resistive layer, with greater thickness to the southwest thinning to the northeast. In addition, the two western areas (C and D), which are both located close to subduction zones, have thicker resistive layers, and the two eastern areas (A and B), which are located farther offshore and closer to the Shatsky Rise, have thinner resistive layers.

Area C is located at the southwestern edge of the present study region and has the thickest resistive layer. The possible thermal structure is more consistent with that expected based on a half space cooling model. This



similarity may imply that the mantle beneath Area C is mostly static and therefore that it has cooled with age through conduction alone without additional dynamic processes. Baba et al. (2010) demonstrated that the temperature should be much lower than the peridotite solidus, even if the amount of water possibly dissolved in olivine is considered. Utada and Baba (2014) indicated that neither silicate melt nor carbonate melt, which can enhance bulk conductivity more than silicate melt, is required to explain the conductivity above ~ 170 km depth.

Area D has a resistive layer that is slightly thinner than that of Area C, but thicker than that predicted from plate cooling models that fit bathymetric subsidence (Parsons and Sclater 1977). Therefore, the mantle here may also

be rather static. However, in the central part of Area D, there is a petit-spot field (Hirano et al. 2006), which is thought to have formed as a result of melt leakage from the asthenosphere through fractures generated by plate bending before subduction. Preliminary results of 3-D inversion analysis of the MT data from Area D revealed a conductive anomaly in the lithospheric mantle beneath the petit-spot field, which suggested melt accumulation and migration to the surface (Baba et al. 2013b). Because carbon dioxide-rich melt is expected from the highly vesicular petit-spot basalt samples (Okumura and Hirano 2013), the mantle beneath the petit-spot field may be relatively enriched in carbon, which may be one of the causes of the difference in the electrical structure of Area D from that of Area C.

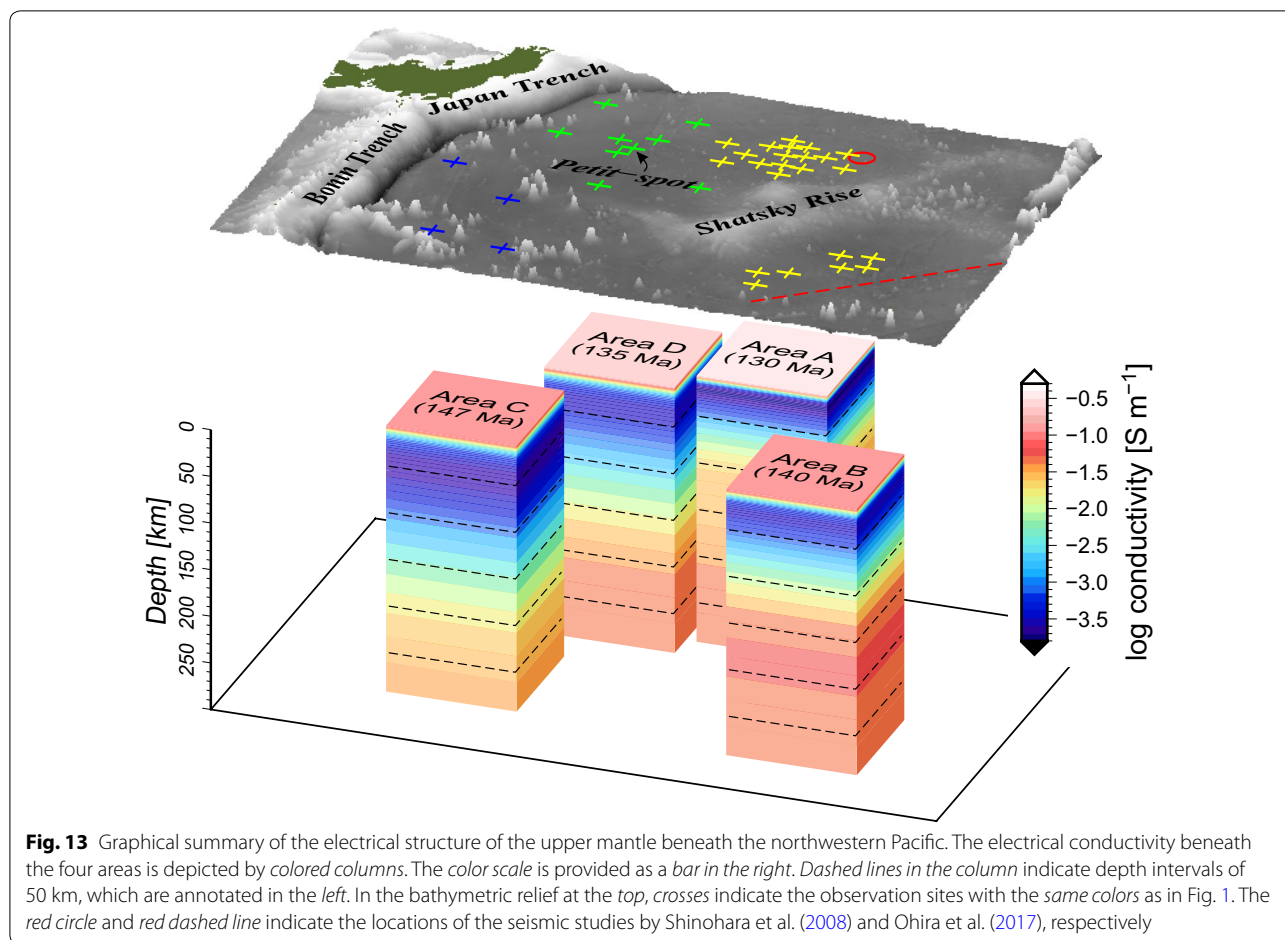


Fig. 13 Graphical summary of the electrical structure of the upper mantle beneath the northwestern Pacific. The electrical conductivity beneath the four areas is depicted by colored columns. The color scale is provided as a bar in the right. Dashed lines in the column indicate depth intervals of 50 km, which are annotated in the left. In the bathymetric relief at the top, crosses indicate the observation sites with the same colors as in Fig. 1. The red circle and red dashed line indicate the locations of the seismic studies by Shinohara et al. (2008) and Ohira et al. (2017), respectively

For Area A and Area B, the plume associated with the formation of the Shatsky Rise may have affected the initial state of the temperature and/or composition of the mantle, although the two areas are located outside of the topographic anomaly of the Shatsky Rise itself. Ohira et al. (2017) found that along the spreading direction southeast of Area B, there are areas where the Moho is diffuse, weak, or absent, and are thus characterized by the presence of a gradual crust–mantle transition in seismic velocity. These authors suggested that the formation time of the crust–mantle transition layer is coincident with that of the Shatsky Rise and inferred a causal relationship. Shinohara et al. (2008) detected a similar crust–mantle transition layer at the eastern edge of Area A. Although they did not propose a geological interpretation of this feature, the same interpretation as that of Ohira et al. may be applicable in this case. The formation of the Shatsky Rise affects both areas, but additional factors are required to explain the differences between Area A and Area B. Note that the effect of the Shatsky Rise cannot be interpreted to represent the rejuvenation concept because it was formed

on the ridge (Nakanishi et al. 1999). Instead, the plume may have promoted small-scale convection locally because of the low viscosity with excess heat and/or volatiles (Argusta et al. 2013). The difference between Area A and Area B may reflect the influence of different parts (i.e., upwelling and downwelling) of convection cells.

Conclusions

The NOMan project completed EM array observations on the seafloor northwest (Area A) and southeast (Area B) of the Shatsky Rise in the northwestern Pacific. The collected data were analyzed based on MT methods, and 1-D electrical conductivity profiles that represent each array were then estimated after topographic effect correction.

The newly acquired data from the NOMan project and the state-of-art analysis enabled us to extend the available period range of MT responses to shorter periods and to evaluate the implication to crustal structure in greater detail than achieved in previous deep ocean MT studies. The difference in the conductivity of the uppermost

layers in Area A and Area B may reflect the difference in the thickness of the sedimentary layer.

We compared the 1-D profiles of the NOMan arrays and two additional areas in the vicinity, off the Bonin Trench (Area C) and off the Japan Trench (Area D). The most remarkable finding is that the thickness of the resistive layer differs significantly for each area. Area A, which we assumed was “normal” in our previous study (Baba et al. 2013a), is not representative of the four areas because the resistive layer is thinnest in this area.

The conductivity structure cannot be explained only by the age difference under a framework of the cooling of thermally conductive, homogeneous mantle. The thermal structure predicted for each area from the plate cooling model for the same plate thickness is almost identical because the lithospheric age is very old and differs only slightly between these areas (from ~130 to ~147 Ma). The significant differences in the thickness of the resistive layer suggest that the thickness of the cool thermal lithosphere is considerably different between these areas to a greater degree than predicted from the global datasets of heat flow and seafloor subsidence. The conductivity of the underlying highly conductive zone is fairly similar between areas, which suggests that the conductive (asthenospheric) mantle is rather uniform, although this zone beneath Area B seems slightly more conductive than those of the other areas.

To explain the observed differences in the thickness of the resistive (lithospheric) layer, it is necessary to introduce dynamic processes. Possible processes may include local, small-scale convection in the asthenosphere and/or influence of the plume associated with the formation of the Shatsky Rise. There is a significant room for further discussion to reach a reasonable and comprehensive interpretation of the lithosphere–asthenosphere system beneath the northwestern Pacific. The present study shows that electrical conductivity information will make significant contributions to such investigation.

Additional files

Additional file 1: Figure S1. MT responses for all sites in Area A and Area B.

Additional file 2: Figure S2. Synthetic inversion tests.

Additional file 3: Table. 1-D electrical conductivity profiles shown in Fig. 11.

Additional file 4: Figure S3. Sounding curves of the scalar MT responses (Z_{det}) and their averages in the four study areas.

Abbreviations

EFOS: electric field observation system; EM: electromagnetic; LAB: Lithosphere–asthenosphere boundary; LAS: lithosphere–asthenosphere system; Ma: million years ago; MBES: multi-narrow beam echo sounding; MT: magnetotelluric; NOMan project: normal oceanic mantle project; OBEM: ocean bottom electromagnetometer; S/N ratio: signal-to-noise ratio; ROV: remotely operated underwater vehicle; 1-D: one-dimensional; 3-D: three-dimensional.

Authors' contributions

KB led all observation, data analysis, and discussion for this study. NT was responsible for the observation using the OBEMs of JAMSTEC and for quality control of the time series data from these devices. TM, PFL, LLZ, and HS contributed to the observations of the NOMan project. NA, NH, and MI contributed to data acquisition in Area D. HU coordinated the NOMan project and supported this research with a grant from the JSPS. All authors contributed to preparation of the manuscript. All authors read and approved the final manuscript.

Author details

¹ Earthquake Research Institute, The University of Tokyo, 1-1-1, Yayoi, Bunkyo-ku, Tokyo 113-0032, Japan. ² Department of Deep Earth Structure and Dynamics Research, Japan Agency for Marine–Earth Science and Technology, 2-15, Natsushima, Yokosuka, Kanagawa 237-0061, Japan. ³ Kobe Ocean Bottom Exploration Center, Kobe University, 5-1-1, Fukaeminami, Higashi-nada-ku, Kobe, Hyogo 658-0022, Japan. ⁴ School of Ocean and Earth Science, Tongji University, 1239 Siping Road, Yangpu District, Shanghai 200-092, China. ⁵ Center for Ocean Drilling Science, Japan Agency for Marine–Earth Science and Technology, 2-15 Natsushima, Yokosuka, Kanagawa 237-0061, Japan. ⁶ Center for Northeast Asian Studies, Tohoku University, 41 Kawauchi, Aoba-ku, Sendai 980-8576, Japan. ⁷ Research Center for Prediction of Earthquakes and Volcanic Eruptions, Graduate School of Science, Tohoku University, 6-6, Aoba, Aramaki, Aoba-ku, Sendai 980-8578, Japan.

Acknowledgements

The authors thank the captains, officers, crew, and ROV operation team of the R/V *KAIRES* of JAMSTEC (for cruises KR10-08, KR11-10, KR12-14, KR14-10, and KR15-14) and the W/V *KAIYU* of Offshore Operation Co., Ltd., for enabling the success of these cruises. Koji Miyakawa, Chikaaki Fujita, Atsushi Watanabe, Takeo Yagi, Toyonobu Ota, Tsukasa Yoshida, Hitoshi Okinaga, Takafumi Kasaya, Misumi Aoki, Kyoko Tanaka, Takeshi Takaesu, Satomi Minamizawa, and Toshikatsu Nasu are also thanked for technical assistance before, during, and after the cruises. The magnetic observatory data for KAK and NWP were provided by the Japan Meteorological Agency website (<http://www.kakioka-jma.go.jp/metadata/>) and the World Data Center for Geomagnetism, Kyoto (<http://wdc.kugi.kyoto-u.ac.jp/>), respectively. Bathymetry data based on MBES were provided by the JAMSTEC Data Site for Research Cruises (<http://www.godac.jamstec.go.jp/darwin/>). Jun Korenaga provided the residual bathymetry data. Heat flow data were acquired from the global heat flow database of the international heat flow commission (<http://www.heatflow.und.edu/>). Comments by two anonymous reviewers yielded improvements in the manuscript. All figures were produced using GMT software (Wessel et al. 2013). This study was partially supported by Grants-in-Aid for Scientific Research (KAKENHI) 22000003, 17340136, and 20340124 from the Japan Society for the Promotion of Science (JSPS).

Competing interests

The authors declare that they have no competing interests.

Availability of data and materials

1-D conductivity profiles supporting the conclusions of this article are included within the article and Additional file 3: Table.

Consent for publication

Not applicable.

Ethics approval and consent to participate

Not applicable.

Funding

Grants-in-Aid for Scientific Research (KAKENHI) 22000003 from the Japan Society for the Promotion of Science (JSPS) supported the acquisition and analysis for the NOMan datasets. Grants-in-Aid for Scientific Research (KAKENHI) 17340136, and 20340124 from the Japan Society for the Promotion of Science (JSPS) supported the acquisition of the OBEM data in Area D.

Publisher's Note

Springer Nature remains neutral with regard to jurisdictional claims in published maps and institutional affiliations.

Received: 30 April 2017 Accepted: 31 July 2017

Published online: 15 August 2017

References

- Abe N, Fujiwara T, Kimura R, Mori A, Ohyama R, Okumura S, Tokunaga W (2013) Trans-Pacific bathymetry survey crossing over the Pacific, Antarctic, and Nazca plates, JAMSTEC Rep. Res Dev 17:43–57. doi:10.5918/jamstecr.17.43
- Amante C, Eakins BW (2009) ETOPO1 1 arc-minute global relief model: procedures, data sources and analysis, NOAA Tech. Memo. NESDIS NGDC-24, National Geophysical Data Center, Marine Geology and Geophysics Division, Boulder, Colorado
- Argusta R, Arcay D, Tommasi A, Davaille A, Ribe N, Gerya T (2013) Small-scale convection in a plume-fed low-viscosity layer beneath a moving plate. *Geophys J Int* 194:591–610. doi:10.1093/gji/ggt128
- Baba K, Chave AD (2005) Correction of seafloor magnetotelluric data for topographic effects during inversion. *J Geophys Res* 110:B12105. doi:10.1029/2004JB003463
- Baba K, Chave AD, Evans RL, Hirth G, Mackie RL (2006a) Mantle dynamics beneath the East Pacific Rise at 17°S: insights from the mantle electromagnetic and tomography (MELT) experiment. *J Geophys Res* 111:B02101. doi:10.1029/2004JB03598
- Baba K, Tarits P, Chave AD, Evans RL, Hirth G, Mackie RL (2006b) Electrical structure beneath the northern MELT line on the East Pacific Rise at 15°45'S. *Geophys Res Lett* 33:L22301. doi:10.1029/2006GL027528
- Baba K, Utada H, Goto T, Kasaya T, Shimizu H, Tada N (2010) Electrical conductivity imaging of the Philippine Sea upper mantle using seafloor magnetotelluric data. *Phys Earth Planet Inter* 183:44–62. doi:10.1016/j.pepi.2010.09.010
- Baba K, Tada N, Zhang L, Liang P, Shimizu H, Utada H (2013a) Is the electrical conductivity of the northwestern Pacific upper mantle normal? *Geochem Geophys Geosyst* 14(12):4969–4979. doi:10.1002/2013GC004997
- Baba K, Abe N, Hirano N, Ichiki M (2013b) Three-dimensional inversion analysis of seafloor magnetotelluric data collected in the northwestern Pacific and implications for the source of petit-spot volcanoes. In: 5th international symposium on three-dimensional electromagnetics, extended abstract
- Baba K, Tada N, Utada H, Siripunvaraporn W (2013c) Practical incorporation of local and regional topography in three-dimensional inversion of deep ocean magnetotelluric data. *Geophys J Int* 194:348–361. doi:10.1093/gji/ggt115
- Burgos G, Montagner J-P, Beucler E, Capdeville Y, Mocquet A, Drilleau M (2014) Oceanic lithosphere–asthenosphere boundary from surface wave dispersion data. *J Geophys Res* 119:1079–1093. doi:10.1002/2013JB010528
- Caldwell TG, Bibby HM, Brown C (2004) The magnetotelluric phase tensor. *Geophys J Int* 158:457–469. doi:10.1111/j.1365-246X.2004.02281.x
- Chave AD, Thomson DJ (2004) Bounded influence magnetotelluric response function estimation. *Geophys J Int* 157:988–1006. doi:10.1111/j.1365-246X.2004.02203.x
- Constable SC, Parker RL, Constable CG (1987) Occam's inversion: a practical algorithm for generating smooth models from electromagnetic sounding data. *Geophysics* 52(3):289–300. doi:10.1190/1.1442303
- Cox CS, Constable SC, Chave AD, Webb SC (1986) Controlled-source electromagnetic sounding of the oceanic lithosphere. *Nature* 320:52–54. doi:10.1038/320052a0
- Dai L, Karato S (2014) High and highly anisotropic electrical conductivity of the asthenosphere due to hydrogen diffusion in olivine. *Earth Planet Sci Lett* 408:79–86. doi:10.1016/j.epsl.2014.10.003
- Evans RL, Hirth G, Baba K, Forsyth D, Chave A, Mackie R (2005) Geophysical evidence from the MELT area for compositional controls on oceanic plates. *Nature* 437:249–252. doi:10.1038/nature04014
- Filloux JH (1977) Ocean-floor magnetotelluric sounding over North Central Pacific. *Nature* 269:297–301. doi:10.1038/269297a0
- Gardés E, Gaillard F, Tarits P (2014) Toward a unified hydrous olivine electrical conductivity law. *Geochem Geophys Geosyst* 15:4984–5000. doi:10.1002/2014GC005496
- Hirano N, Takahashi E, Yamamoto J, Abe N, Ingle SP, Kaneoka I, Hirata T, Kimura J, Ishii T, Ogawa Y, Machida S, Suyehiro K (2006) Volcanism in response to plate flexure. *Science* 313:1426–1428. doi:10.1126/science.1128235
- Hirschmann MM (2010) Partial melt in the oceanic low velocity zone. *Phys Earth Planet Inter* 179:60–71. doi:10.1016/j.pepi.2009.12.003
- Isse T, Shiobara H, Yoshizawa K, Kawakatsu H, Sugioka H, Ito A, Suetsugu D, Utada H (2017) Upper mantle structure beneath the Pacific Ocean revealed by land and seafloor broadband observations. *JpGU-AGU Joint Meeting 2017, Abstract, SIT25-05*
- Kawakatsu H, Utada H (2017) Seismic and electrical signatures of the lithosphere–asthenosphere system of the normal oceanic mantle. *Ann Rev Earth Planet Sci*. doi:10.1146/annurev-earth-063016-020319
- Kawakatsu H, Kumar P, Takei Y, Shinohara M, Kanazawa T, Araki E, Suyehiro K (2009) Seismic evidence for sharp lithosphere–asthenosphere boundaries of oceanic plates. *Science* 324:499–502. doi:10.1126/science.1169499
- Korenaga T, Korenaga J (2008) Subsidence of normal lithosphere, apparent thermal expansivity, and seafloor flattening. *Earth Planet Sci Lett* 268:41–51. doi:10.1016/j.epsl.2007.12.022
- Maggi A, Debayle E, Priestley K, Barruol G (2006) Multimode surface waveform tomography of the Pacific Ocean: a closer look at the lithospheric cooling signature. *Geophys J Int* 166:1384–1397. doi:10.1111/j.1365-246X.2006.03037.x
- Matsuno T, Suetsugu D, Baba K, Tada N, Shimizu H, Shiobara H, Isse T, Sugioka H, Ito A, Obayashi M, Utada H (2017) Mantle transition zone beneath a normal seafloor in the northwestern Pacific: electrical conductivity, seismic thickness, and water content. *Earth Planet Sci Lett* 462:189–198. doi:10.1016/j.epsl.2016.12.045
- Müller RD, Sdrolias M, Gaina C, Roest WR (2008) Age, spreading rates, and spreading asymmetry of the world's ocean crust. *Geochem Geophys Geosyst* 9(4):Q04006. doi:10.1029/2007GC001743
- Naif S, Key K, Constable S, Evans RL (2013) Melt-rich channel observed at the lithosphere–asthenosphere boundary. *Nature* 495:356–359. doi:10.1038/nature11939
- Nakanishi M, Tamaki K, Kobayashi K (1992) A new Mesozoic isochrone chart of the northwestern Pacific Ocean: paleomagnetic and tectonic implications. *Geophys Res Lett* 19(7):693–696. doi:10.1029/92GL00022
- Nakanishi M, Sager W, Klaus A (1999) Magnetic lineations within Shatsky Rise, northwest Pacific Ocean: implications for hot spot-triple junction interaction and oceanic plateau formation. *J Geophys Res* 104(B4):7539–7556. doi:10.1029/1999JB900002
- Nettles M, Dziewoński AM (2008) Radially anisotropic shear velocity structure of the upper mantle globally and beneath North America. *J Geophys Res* 113:B02303. doi:10.1029/2006JB004819
- Ohira A, Kodaira S, Nakamura Y, Fujie G, Arai R, Miura S (2017) Structural variation of the oceanic Moho in the Pacific plate revealed by active-source seismic data. *Earth Planet Sci Lett* (Accepted)
- Okumura S, Hirano N (2013) Carbon dioxide emission to Earth's surface by deep-sea volcanism. *Geology* 41(11):1167–1170. doi:10.1130/G34620
- Parsons B, Sclater JG (1977) An analysis of the variation of ocean floor bathymetry and heat flow with age. *J Geophys Res* 82(5):803–827. doi:10.1029/JB082i005p00803
- Pommier A, Kohlstedt DL, Qi C, Garnero EJ, Mackwell SJ, Tyburczy JA (2015) Experimental constraints on the electrical anisotropy of the lithosphere–asthenosphere system. *Nature* 522:202–206. doi:10.1038/nature14502
- Richter FM (1973) Convection and the large-scale circulation of the mantle. *J Geophys Res* 78(35):8735–8745. doi:10.1029/JB078i035p08735
- Rung-Arunwan T, Siripunvaraporn W, Utada H (2016) On the Berdichevsky average. *Phys Earth Planet Inter* 253:1–4. doi:10.1016/j.pepi.2016.01.006
- Sager WW (2005) What built Shatsky Rise, a mantle plume or ridge tectonics? In: Foulger GR, Natland JH, Presnall DC, Anderson DL (eds) Plates, plumes, and paradigms. Geological Society of America Special Paper 388, pp 721–733. doi:10.1130/2005.2388(41)
- Shimizu H, Yoneda A, Baba K, Utada H, Palshin NA (2011) S_q effect on the electromagnetic response functions in the period range between 10^4 and 10^5 s. *Geophys J Int* 186:193–206. doi:10.1111/j.1365-246X.2011.05036.x
- Shinohara M, Fukano T, Kanazawa T, Araki E, Suyehiro K, Mochizuki M, Nakahigashi K, Yamada T, Mochizuki K (2008) Upper mantle and crustal structure beneath the Northwestern Pacific Basin using a seafloor borehole broadband seismometer and ocean bottom seismometers. *Phys Earth Planet Sci* 170:95–106. doi:10.1016/j.pepi.2008.07.039
- Sifré D, Gardés E, Massuyeau M, Hashim L, Hier-Majumder S, Gaillard F (2014) Electrical conductivity during incipient melting in the oceanic low-velocity zone. *Nature* 509:81–85. doi:10.1038/nature13245

- Smith WHF, Sandwell DT (1997) Global seafloor topography from satellite altimetry and ship depth soundings. *Science* 277:1956–1962. doi:[10.1126/science.277.5334.1956](https://doi.org/10.1126/science.277.5334.1956)
- Stein CA, Stein S (1992) A model for the global variation in oceanic depth and heat flow with lithospheric age. *Nature* 359:123–129. doi:[10.1038/359123a0](https://doi.org/10.1038/359123a0)
- Swift Jr CM (1967) A magnetotelluric investigation of an electrical conductivity anomaly in the southwestern United States. Ph.D. thesis, Massachusetts Institute of Technology
- Tada N, Baba K, Utada H (2014) Three-dimensional inversion of seafloor magnetotelluric data collected in the Philippine Sea and the western margin of the northwest Pacific Ocean. *Geochem Geophys Geosyst* 15:2895–2917. doi:[10.1002/2014GC005421](https://doi.org/10.1002/2014GC005421)
- Toh H, Hamano Y, Ichiki M (2006) Long-term seafloor geomagnetic station in the northwest Pacific: a possible candidate for a seafloor geomagnetic observatory. *Earth Planets Space* 58:697–705. doi:[10.1186/BF03351970](https://doi.org/10.1186/BF03351970)
- Turcotte DL, Schubert G (2002) *Geodynamics*, 2nd edn. Cambridge University Press, Cambridge
- Utada H, Baba K (2014) Estimating the electrical conductivity of the melt phase of a partially molten asthenosphere from seafloor magnetotelluric sounding data. *Phys Earth Planet Inter* 227:41–47. doi:[10.1016/j.pepi.2013.12.004](https://doi.org/10.1016/j.pepi.2013.12.004)
- Utada H, Baba K, Shimizu H, Shiobara H, Tada N (2013) Ocean bottom measurements of the Earth's electric field using long cable installed by ROV. In: *Proceedings of the international symposium on underwater technology*. IEEE, Tokyo
- Wang D, Mookherjee M, Xu Y, Karato S (2006) The effect of water on the electrical conductivity of olivine. *Nature* 443:977–980. doi:[10.1038/nature05256](https://doi.org/10.1038/nature05256)
- Wessel P, Smith WHF, Scharroo R, Luis J, Wobbe F (2013) Generic mapping tools: improved version released. *Eos Trans AGU* 94(45):409–420
- Yoshino T, Matsuzaki T, Shatskiy A, Katsura T (2009) The effect of water on the electrical conductivity of olivine aggregates and its implications for the electrical structure of the upper mantle. *Earth Planet Sci Lett* 288:291–300. doi:[10.1016/j.epsl.2009.09.032](https://doi.org/10.1016/j.epsl.2009.09.032)
- Zhang B, Yoshino T, Yamazaki D, Manthilake G, Katsura T (2014) Electrical conductivity anisotropy in partially molten peridotite under shear deformation. *Earth Planet Sci Lett* 405:98–109. doi:[10.1016/j.epsl.2014.08.018](https://doi.org/10.1016/j.epsl.2014.08.018)

Submit your manuscript to a SpringerOpen[®] journal and benefit from:

- Convenient online submission
- Rigorous peer review
- Open access: articles freely available online
- High visibility within the field
- Retaining the copyright to your article

Submit your next manuscript at ► springeropen.com
